NASA/CR—2015-218854

Understanding and Mitigating Tip Leakage and Endwall Losses in High Pressure Ratio Cores

Jesse Christophel
Pratt & Whitney, East Hartford, Connecticut

August 2015

NASA STI Program . . . in Profile

Since its founding, NASA has been dedicated to the advancement of aeronautics and space science. The NASA Scientific and Technical Information (STI) Program plays a key part in helping NASA maintain this important role.

The NASA STI Program operates under the auspices of the Agency Chief Information Officer. It collects, organizes, provides for archiving, and disseminates NASA's STI. The NASA STI Program provides access to the NASA Technical Report Server—Registered (NTRS Reg) and NASA Technical Report Server—Public (NTRS) thus providing one of the largest collections of aeronautical and space science STI in the world. Results are published in both non-NASA channels and by NASA in the NASA STI Report Series, which includes the following report types:

- TECHNICAL PUBLICATION. Reports of completed research or a major significant phase of research that present the results of NASA programs and include extensive data or theoretical analysis. Includes compilations of significant scientific and technical data and information deemed to be of continuing reference value. NASA counter-part of peer-reviewed formal professional papers, but has less stringent limitations on manuscript length and extent of graphic presentations.

- TECHNICAL MEMORANDUM. Scientific and technical findings that are preliminary or of specialized interest, e.g., "quick-release" reports, working papers, and bibliographies that contain minimal annotation. Does not contain extensive analysis.

- CONTRACTOR REPORT. Scientific and technical findings by NASA-sponsored contractors and grantees.

- CONFERENCE PUBLICATION. Collected papers from scientific and technical conferences, symposia, seminars, or other meetings sponsored or co-sponsored by NASA.

- SPECIAL PUBLICATION. Scientific, technical, or historical information from NASA programs, projects, and missions, often concerned with subjects having substantial public interest.

- TECHNICAL TRANSLATION. English-language translations of foreign scientific and technical material pertinent to NASA's mission.

For more information about the NASA STI program, see the following:

- Access the NASA STI program home page at http://www.sti.nasa.gov

- E-mail your question to help@sti.nasa.gov

- Fax your question to the NASA STI Information Desk at 757-864-6500

- Telephone the NASA STI Information Desk at 757-864-9658

- Write to:
  NASA STI Program
  Mail Stop 148
  NASA Langley Research Center
  Hampton, VA 23681-2199

NASA/CR—2015-218854

Understanding and Mitigating Tip Leakage and Endwall Losses in High Pressure Ratio Cores

Jesse Christophel
Pratt & Whitney, East Hartford, Connecticut

Prepared under Contract NNC10BA12B, Task order NNC11TA41T

National Aeronautics and
Space Administration

Glenn Research Center
Cleveland, Ohio 44135

August 2015

This report contains preliminary findings, subject to revision as analysis proceeds.

This work was sponsored by the Fundamental Aeronautics Program at the NASA Glenn Research Center.

Level of Review: This material has been technically reviewed by NASA technical management.

Available from

NASA STI Program
Mail Stop 148
NASA Langley Research Center
Hampton, VA 23681-2199

National Technical Information Service
5285 Port Royal Road
Springfield, VA 22161
703-605-6000

This report is available in electronic form at http://www.sti.nasa.gov/ and http://ntrs.nasa.gov/

Understanding and Mitigating Tip Leakage and Endwall Losses in High Pressure Ratio Cores

Jesse Christophel
Pratt & Whitney
East Hartford, Connecticut 06108

ABSTRACT

Reducing endwall and tip secondary flow losses will be a key enabler for the next generation of commercial and military air transport and will be an improvement on the state-of-the-art in turbine loss reduction strategies.

The objective of this research is three-fold:

1) To improve understanding of endwall secondary flow and tip clearance losses
2) To develop novel technologies to mitigate these losses and test them in low-speed cascade and rig environments
3) To validate predictive tools

To accomplish these objectives, Pratt & Whitney (P&W) has teamed with Pennsylvania State University (PSU) to experimentally test new features designed by P&W. P&W will create new rim-cavity features to reduce secondary flow loss and improve purge flow cooling effectiveness and new blade tip features to manage leakage flows and reduce tip leakage secondary flow loss. P&W is currently developing technologies in these two areas that expect to be assimilated in the N+2/N+3 generation of commercial engines.

INTRODUCTION

P&W has designed a single stage, high pressure turbine for testing in the Axial Flow Turbine Research Facility (AFTRF). This design differs from an engine because the test facility is low-speed and low-temperature. The AFTRF test turbine has also been scaled up relative to the engine to allow for better spatial resolution.

After designing the airfoils for the AFTRF, additional changes were made to suit the geometry to the Low Speed Cascade (LSC). These changes include scaling up by 3X (relative to the AFTRF) to fit the cascade dimensions, transforming the 3D vane into a 2D geometry, and replacing the blade with an elliptical bluff body that will represent the pressure distortion imposed on the rim cavity flow by a blade.

The purpose of this final technical report is to summarize key findings from work completed during NRA contract NNC10BA12B, task order NNC11TA41T (August 2011 – December 2014). This work was completed by the primary contract holder, Pratt & Whitney, and the subcontractor, The Pennsylvania State University. Additional test results and details are included in the attachments, which contain the university thesis documents written by the students performing this contract work.

TECHNICAL DISCUSSION

1 Facility overview

Testing under this NRA occured in two separate but complimentary facilities. The first is the AFTRF, which is a low-speed rig. This facility allows for steady and unsteady measurements in the static and rotating frame of reference. These measurements are critical to understanding the unsteady wakes and secondary flow structures that result from blade tip and rim cavity leakage flow. A cross-section of the AFTRF is shown in Figure 1. Flow enters through a bell-mouth inlet, passes through the single-stage turbine, and then exits through a guide vane. The geometry shown in this cross section is from previous testing and does not represent the P&W hardware.

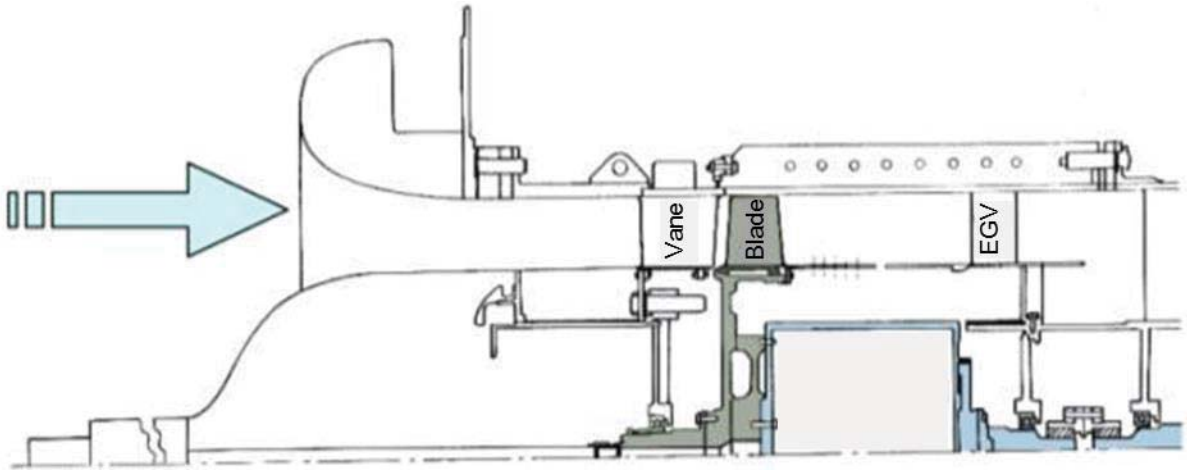

Figure 1: Axial Flow Turbine Research Facility Cross Section

The second facility is the LSC, which is a re-circulating wind tunnel with a removable test section located at one corner. This cascade is larger scale than the AFTRF which allows for greater measurement resolution. Because of the stationary nature of the cascade, it allows for a focused study on endwall and rim cavity flow structures. To represent the effect of a passing blade in the engine environment, a bluff body will be positioned downstream of the rim cavity. This will allow for the simulation of an instantaneous blade clocking position while measuring purge effectiveness and characterizing the flow field where the purge flow interacts with the mainstream. Because of the relative ease of testing and lower cost associated with the LSC, many geometries can be tested, and only the most promising will be installed in the AFTRF for rotating tests. An overview of the LSC is shown in Figure 2.

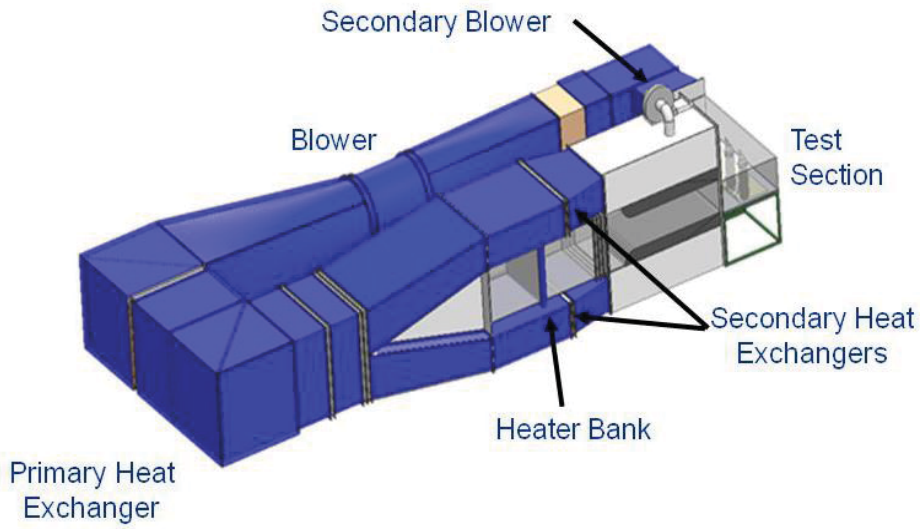

Figure 2: Low Speed Cascade Wind Tunnel Overview

Test Geometries

A comparison of the AFTRF and LSC cross sections is shown in Figure 3. Note that in this image the cross sections have been scaled to the same size. This figure shows the similarity in geometry between the AFTRF and LSC.

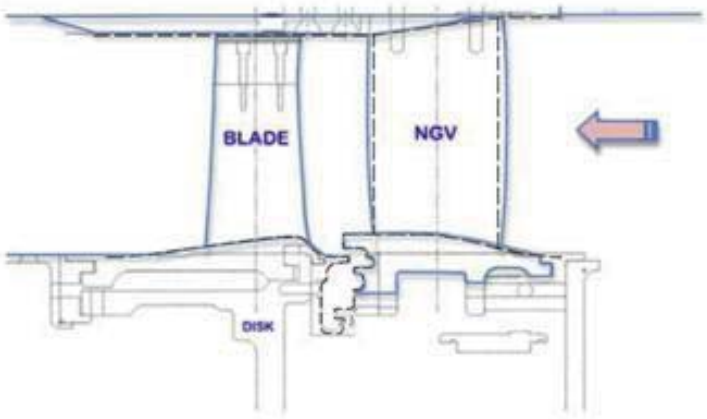

Figure 3: AFTRF (solid) and LSC (dashed) Cross Section Overlay

The rim cavity shown in Figure 3 is a basic overlapping seal where the vane platform trailing edge overlaps the blade platform leading edge. The purge flow enters at the bottom through an opening created by a typical knife-edge engine seal. In the AFTRF, this seal gap will be measured and controlled and in the LSC a simple slot opening will be used to introduce the air.

The test vane is based on a modern design for high pressure turbine first stage vanes. The LSC vane has a constant cross section based on the 25% span cross section of the AFTRF vane. A solid line on the AFTRF vane in Figure 4 shows where the LSC vane cross section comes from.

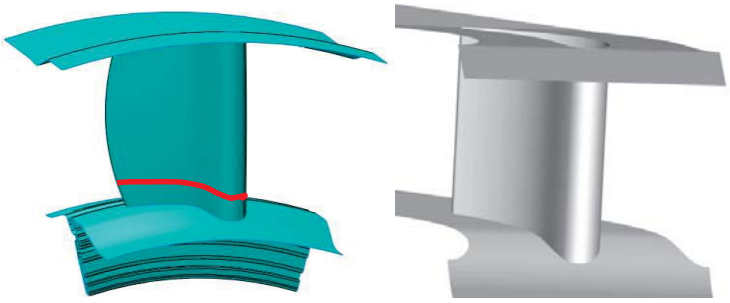

Figure 4: AFTRF (left) and LSC (right) Vane Geometry

A summary of the scaling parameters considered and final design values for the test vanes is given in Table 1. A scale factor for the LSC of 3.0, relative to the AFTRF geometry, was chosen based on the constraints of wind tunnel flow capability and required number of vanes to ensure flow periodicity. For both test vanes, the inlet Reynolds number was maintained. The inlet velocity, exit velocity, and flow angle are mass averaged values obtained from steady RANS CFD of both the LSC and the AFTRF. The flow angle values are at a streamwise location 10% axial chord downstream of the vane trailing edge.

Table 1: Scaling Parameters and Design Summary

	AFTRF Facility	Linear Cascade (using R ~ 0.25S_{TE})
V_{in} [ft/s]	101.00	34.1
C_{ax} [in]	2.6	7.8
S_0 [in]	5.0	14.9
$Re_{inlet,Cax}$	127,828	129,739
V_{exit} [ft/s]	470.6	145.3
$Re_{exit,Cax}$	546,300	552640
TW [in]	0.86	2.67
P [in]	3.16	9.49
S_{TE} [in]	4.1	12.3
P/TW	3.62	3.55
S_0/S_{TE}	1.22	1.22
V_{exit}/V_{in}	4.7	4.3
Flow Angle	72.0°	71.2°

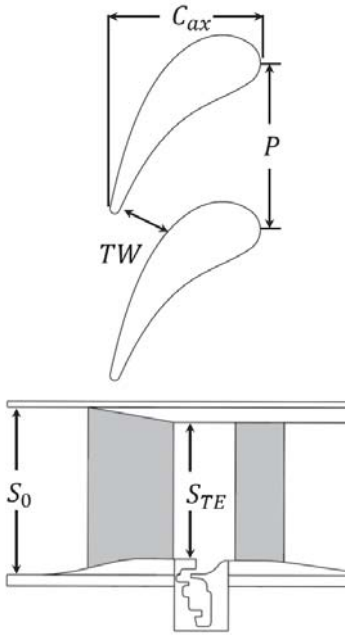

Figure 5 shows the surface static pressure distribution for the two vanes as well as a vane cross section at 25% span. The pressure distributions from the LSC and AFTRF were obtained from the same steady RANS CFD as the flow parameters listed above in Table 1. These cross sections have been scaled to the same axial chord for easier comparison. As the figure shows, there has been a minor change to the LSC vane cross section to account for the incompressible flow environment.

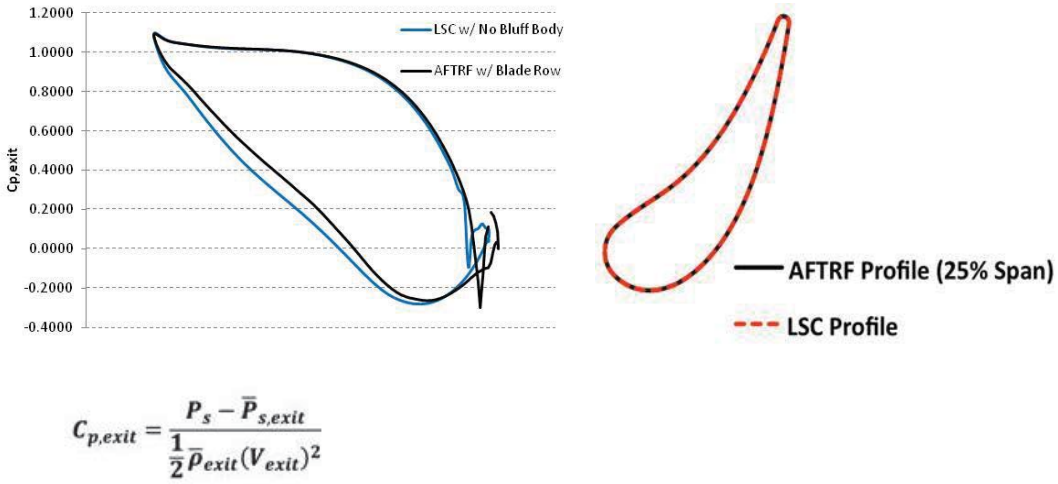

$$C_{p,exit} = \frac{P_s - \bar{P}_{s,exit}}{\frac{1}{2}\bar{\rho}_{exit}(V_{exit})^2}$$

Figure 5: Vane Cross Section and Pressure Distribution Comparison

Additional checks on the vane design were to match the vane wake pressure distortion imposed on the rim cavity. This pressure distortion greatly affects the flow near the rim seal exit, which is the area of concern for these tests. Figure 6 shows a comparison between the AFTRF and the LSC taken at 10% and 25% span on a plane located at the rim cavity leading edge. The figures on the right show the axial plane and the various span values from which the vane wake pressure distributions were taken. The plot on the left is of local pressure coefficient at various spans. The pressure distribution was non-dimensionalized using mass-averaged reference values from the plane and spans at which the pressure distribution was taken. This local pressure coefficient allows the comparison of the annular AFTRF facility and the linear LSC, which appears very similar. Slight differences are seen between the two cases in which the LSC has a slightly smaller difference between the maximum and minimum values of the pressure coefficient distribution. Figure 6 illustrates that the vane wake pressure distortion at the rim seal exit is very similar between the two facilities.

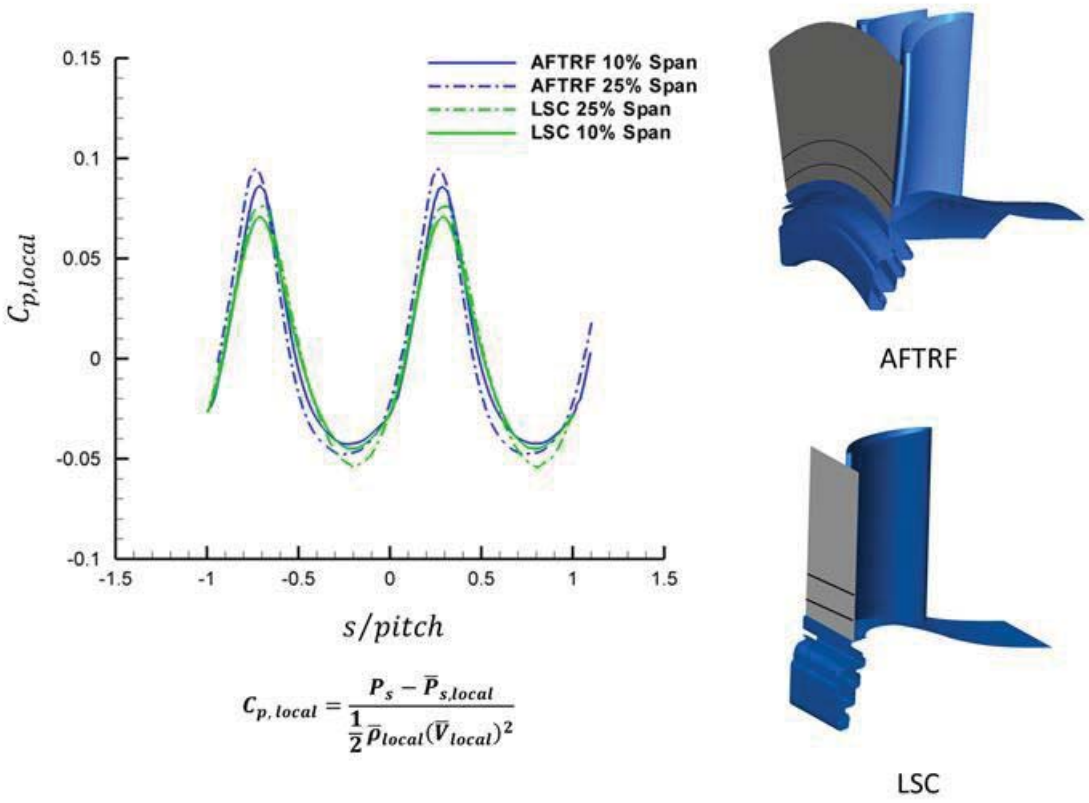

Figure 6: Test Vane Pressure Distortion at Rim Cavity Edge

The test blade is based on a modern design for high pressure turbine first stage blades. An image of the AFTRF test blade is shown in Figure 7. This blade was designed so that the tip and endwall sections are replaceable. This will allow for easy changes of test geometry.

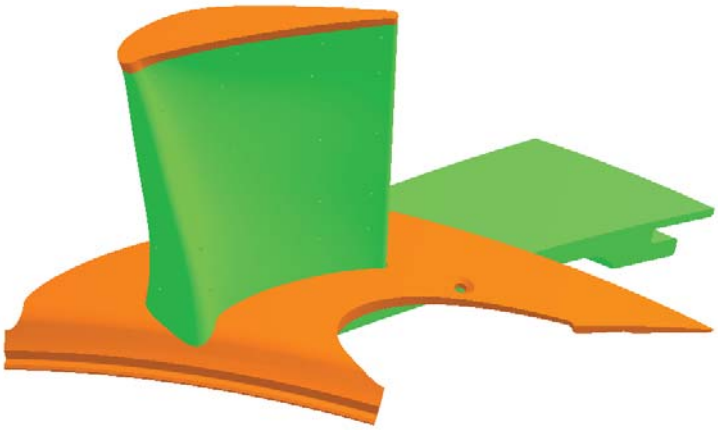

Figure 7: AFTRF Blade Geometry

Figure 8shows the surface static pressure distribution for the AFTRF blade as well as a blade cross section at 25% span.

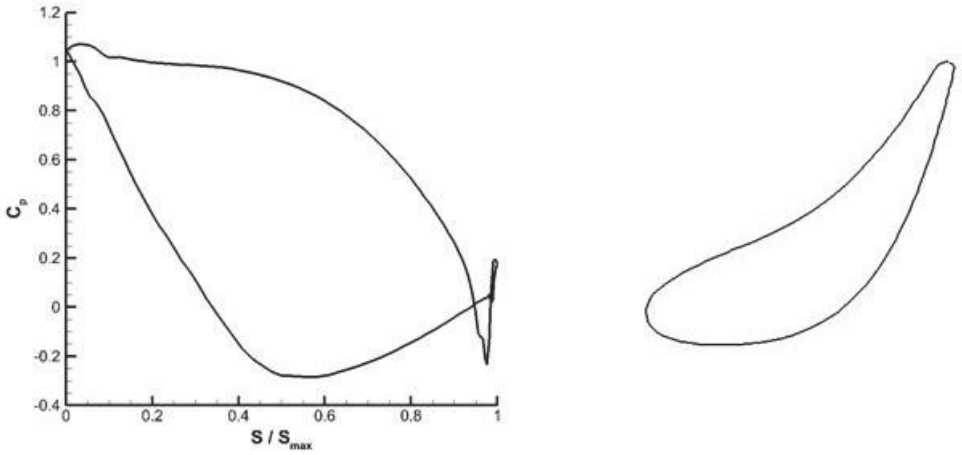

Figure 8: Vane Cross Section and Pressure Distribution

For the LSC, a bluff body design was chosen from available NACA airfoils to provide the correct upstream pressure distortion that the blade imposes on the rim-cavity. A cross-section of the bluff body, as installed in the LSC is shown in Figure 9. As you can see, the stationary bluff bodies are relatively small compared to the vane or a traditional blade.

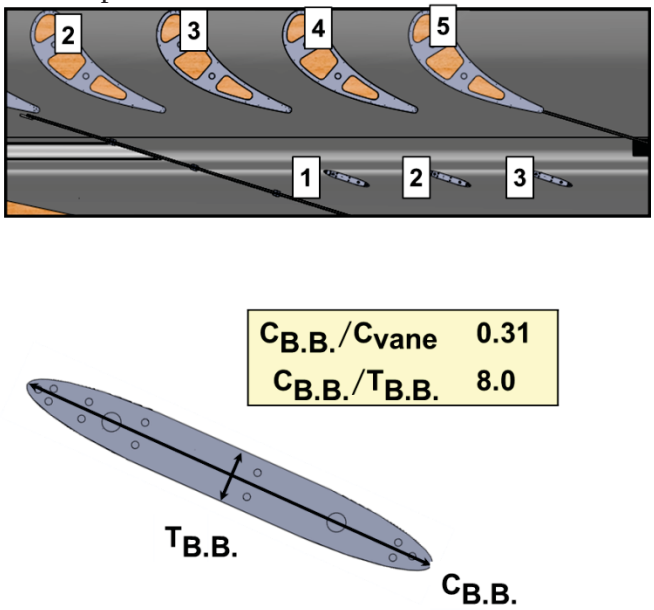

Figure 9: LSC Bluff Bodies

The pressure distortion from the AFTRF blade and the LSC bluff bodies are compared in Figure 10. The two plots of pressure are taken at the rim-cavity leading edge and trailing edge and this figure shows that the LSC bluff bodies have excellent representation of the upstream pressure effect on the rim-cavity due to the downstream blade.

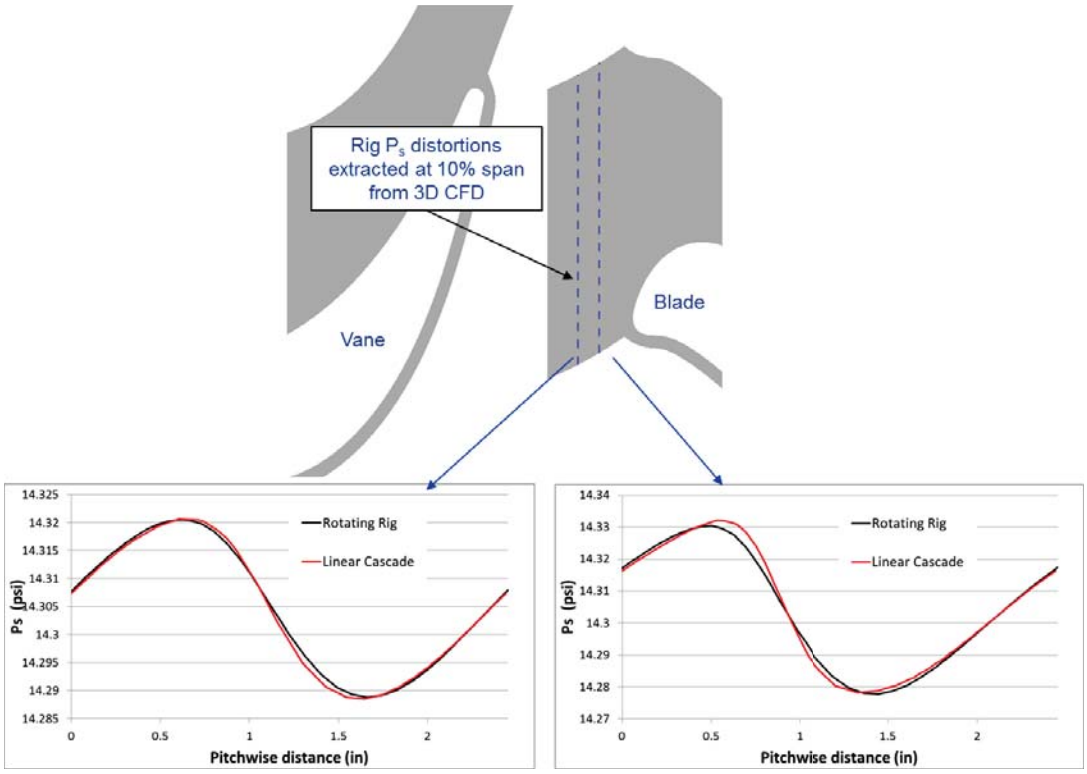

Figure 10: Rim-Cavity Static Pressure Distortion Due to AFTRF Blade and LSC Bluff Body

P&W and PSU have created a single-stage turbine design for the AFTRF and the LSC that have matched aerodynamic characteristics for the two facility operating parameters. The inlet Reynolds number and stage pressure ratios are matched, the vane pressure distributions are matched, and the rim-cavity static pressure field is matched with the presence of a downstream blade or bluff body.

Based on this, the two experimental facilities have been set-up correctly to perform testing on similar geometries.

2 Low speed cascade

The test section for the LSC is shown in Figure 11. In this image, you can see the five vane leading edges and four central flow paths. The outer flow paths are controlled with flexible walls and by-pass tubes to help balance the flow evenly through the four central passages.

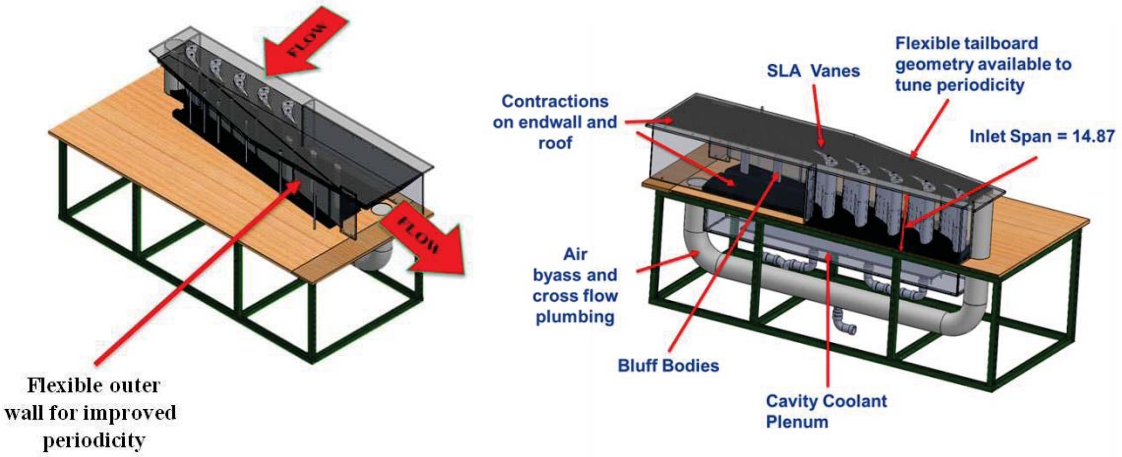

Figure 11: NRA Test Section Used in the LSC

To overcome the static nature of the LSC test and get adequate periodicity in the rim-cavity, a cross-flow loop was installed to represent the circumferential flow created by a spinning disk and blade in the rotating environment. This cross-flow was metered and controlled to provide periodic pressure boundary conditions at the rim-cavity exit and is separate from the rim-cavity purge exit flow. Figure 12 shows a cross-section of the LSC rim-cavity with the cross flow inlet and exit as well as a photograph of the cross-flow loop.

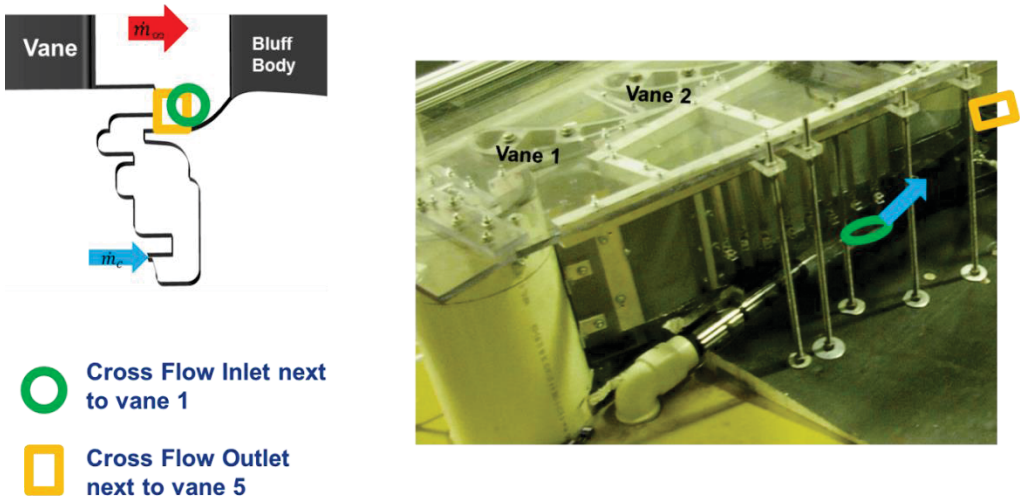

Figure 12: LSE Test Section Showing Cross-Flow Loop

The vane endwall and downstream rim cavity geometry were manufactured with expanded polystyrene foam, shown in Figure 13. The manufacturing method permitted each component to be cut from one piece, resulting in accurate geometry definition. The downside of this material

is that the surface is much rougher, so a low conductivity paste, called “Temp-Coat 101” was applied to the surface to achieve the desired smoothness.

Figure 13: Downstream Side of Rim Cavity and Endwall
Made With Expanded Polystyrene Foam

Instrumentation of LSC Hardware

Below is a comprehensive list of instrumentation on the LSC:

1. Boundary condition measurements
    a. Inlet velocity profile (Pitot probe)
    b. Inlet temperature profile (probe-mounted thermocouple)
    c. Vane surface static pressure to ensure periodicity (surface mounted static pressure taps)
    d. Bluff body surface static pressure to ensure periodicity (surface mounted static pressure taps)
    e. Coolant pressure and temperature (plenum mounted static pressure tap and thermocouples)
    f. Coolant flow rate (in-line venturi meter)
    g. Cross flow inlet and exit temperature (to ensure no heat-up or cool-down of cross flow during return loop)
    h. Cross flow rate (in-line venture meter)
2. Aerodynamic losses
    a. Downstream total pressure (5-hole pressure probe)
3. Rim cavity effectiveness
    a. Endwall adiabatic film effectiveness (IR camera)
    b. Purge flow temperature (rim seal thermocouple rakes)
    c. Seal effectiveness with species tracking (CO2 sniffers)
4. Main stream flow field
    a. 2D flow field measurements (PIV measurement system)

The row of vane static pressure taps was built into each vane at the mid span location. These taps will be used to provide benchmark information as well as obtain vane to vane pressure field periodicity. The static pressure taps were built into the SLA models so that instrumentation

connections could be more easily made below the test section end wall. The LSC vanes and static pressure taps are shown in Figure 14.

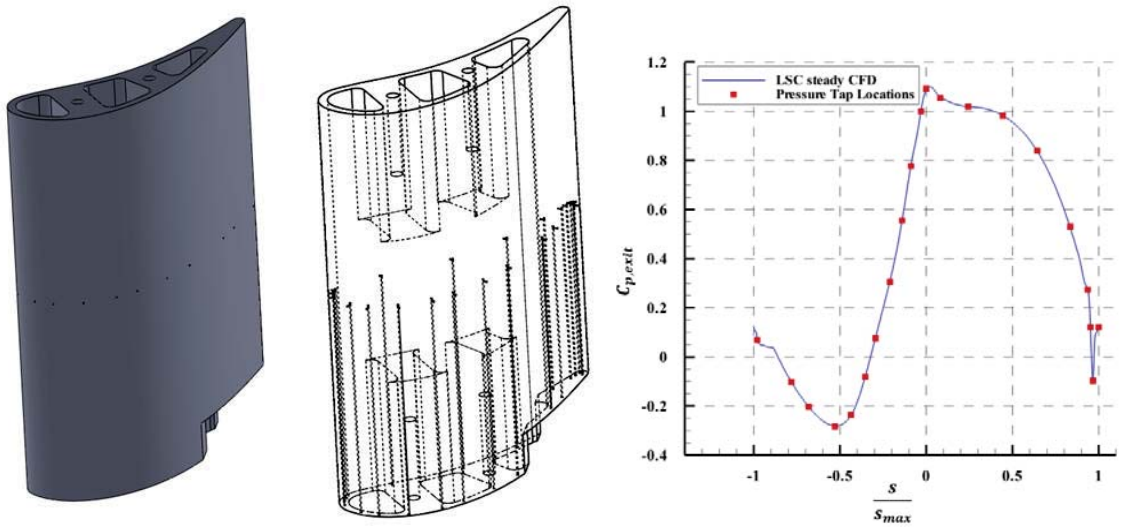

Figure 14: LSC Vane Showing Static Pressure Tap Holes

Rim cavity measurement locations are shown in Figure 15. Thermocouple rakes and pressure taps are be placed in the seal cavity over two vane pitches at an interval of 20% of the vane pitch. These measurements will complement the surface IR measurements of adiabatic wall temperature on the mainstream endwalls to determine rim cavity flow effectiveness.

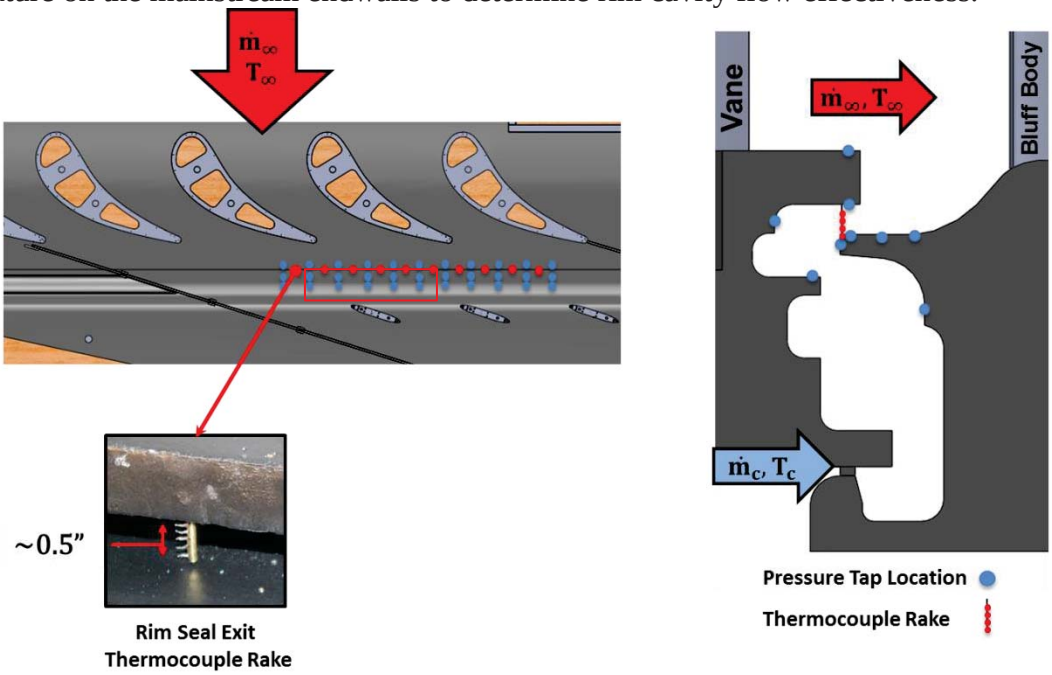

Figure 15: LSC Rim Cavity Pressure and Temperature Measurements. Red rectangle in top down view represents regions if IR camera thermography.

Aerodynamic loss is measured using a five-hole pressure probe downstream of the vane row. The probe and approximate measurement location is shown in Figure 16. The necessary inlet total pressure and velocity needed for this loss calculation will be monitored throughout testing as it is necessary to confirm uniform, steady state inlet conditions.

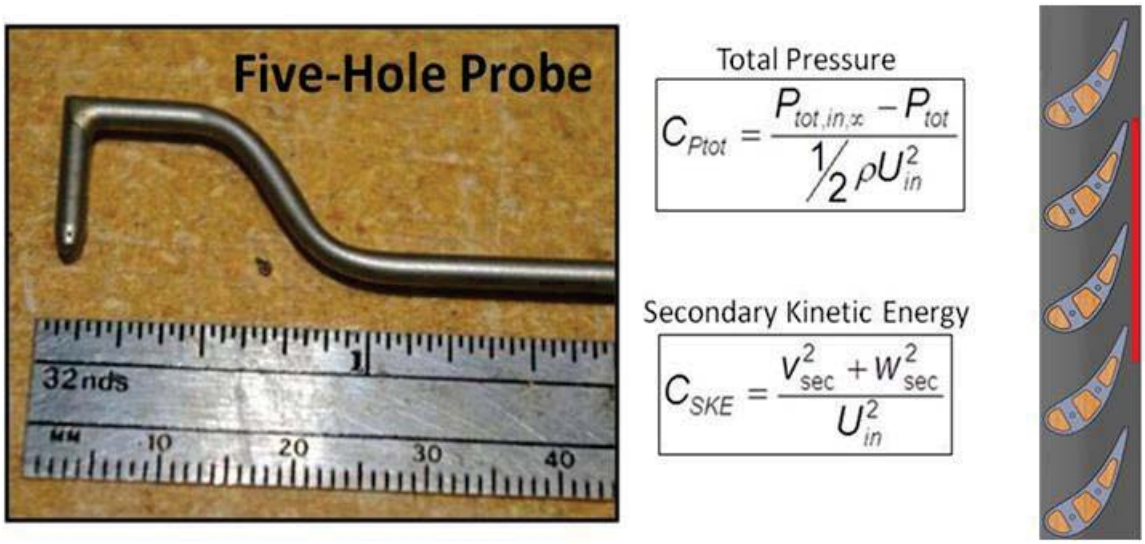

Figure 16: LSC Five-Hole Pressure Probe and Measurement Location

The rim-cavity CO2 measurement ports are shown in Figure 17. Existing static pressure taps were connected to a CO2 sniffer for these measurements.

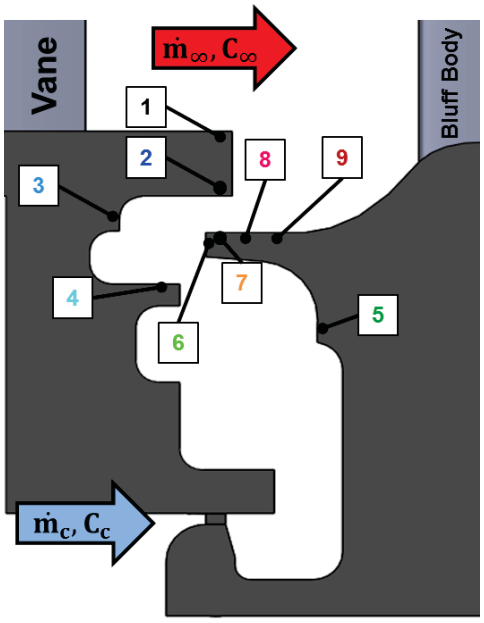

Figure 17: LSC Rim-Cavity Static Pressure Tap and CO2 Measurement Locations

The LDV measurement planes are shown in Figure 18. The LDV system uses two cameras (stereo-PIV) to capture all three components of velocity within the plane of measurement.

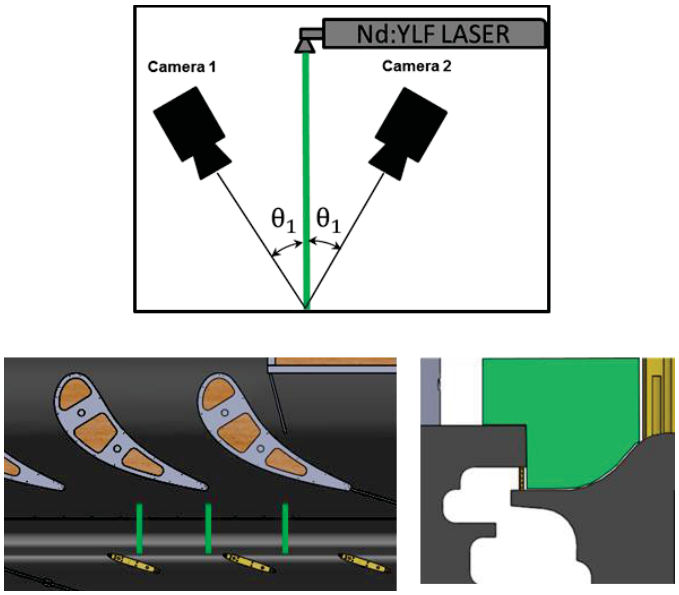

Figure 18: LSC Rim-Cavity Stereo PIV Measurement Planes

The LSC test section has been designed with adequate controls for ensuring periodic flow through the vanes, over the rim-cavity, and through the bluff bodies. Main stream flow and purge flow are both monitored and controlled and rim-cavity cross-flow is controlled to ensure periodic rim-seal boundary conditions.

Low Speed Cascade Results

Initial testing of the vane cascade involved characterizing the static pressure distribution on the vanes at mid-span to ensure that periodic flow occurred in the mainstream. Figure 19 shows good periodicity among the vanes in the test section with and without the purge flow.

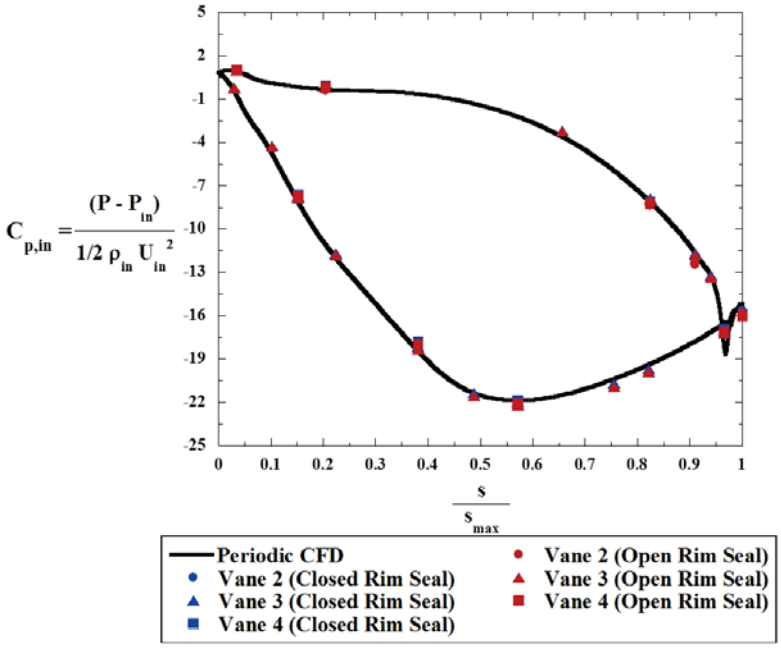

Figure 19. Mid-span pressure distribution on vanes with and without the rim seal

Static pressure distributions on the endwall with no purge flow agreed well with that predicted from computational fluid dynamics (CFD) from both a periodic solution as well as a five-vane solution. Those results are shown in Figure 20 with good agreement between the experiments and both CFD solutions over the majority of the passages. The static pressure measurements were made from a point just downstream of the vanes and upstream of the seal (labelled tap 1 in Figure 17).

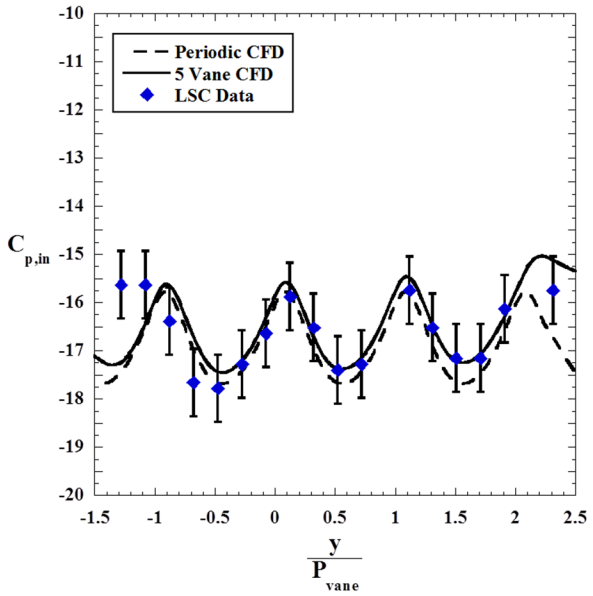

Figure 20. Comparison of vane endwall pressure distribution from the LSC and CFD predictions

In a gas turbine engine, tangential flow is induced in the seals resulting from the swirl in the mainstream created by the vanes and the rotation of the downstream rotor. Since the experiments conducted in the LSC are static experiments, it was necessary to simulate the cross-flow that actually occurs in the operating engine. In addition, initial static pressure measurements on the platform in the seal region indicated a strong aperiodic behavior of the flow exiting the seal. The aperiodicity was verified using (CFD) simulations replicating the five vane test section with the finite number of vanes. Those aperiodic results are shown in Figure 21 where the streamlines are colored by the fluid temperature, which is also used to quantify the sealing effectiveness:

$$\bar{\varepsilon}_c = \frac{T_\infty - \bar{\bar{T}}}{T_\infty - T_c}$$

Figure 21 indicates that there is a fluid build-up on the inner wall (top side of figure) which is influenced by the external cross-flow and the vane turning. To alleviate the aperiodic behavior and more closely simulate that which occurs in a turbine with multiple passages, a cross-flow loop was designed through the use of continued CFD studies.

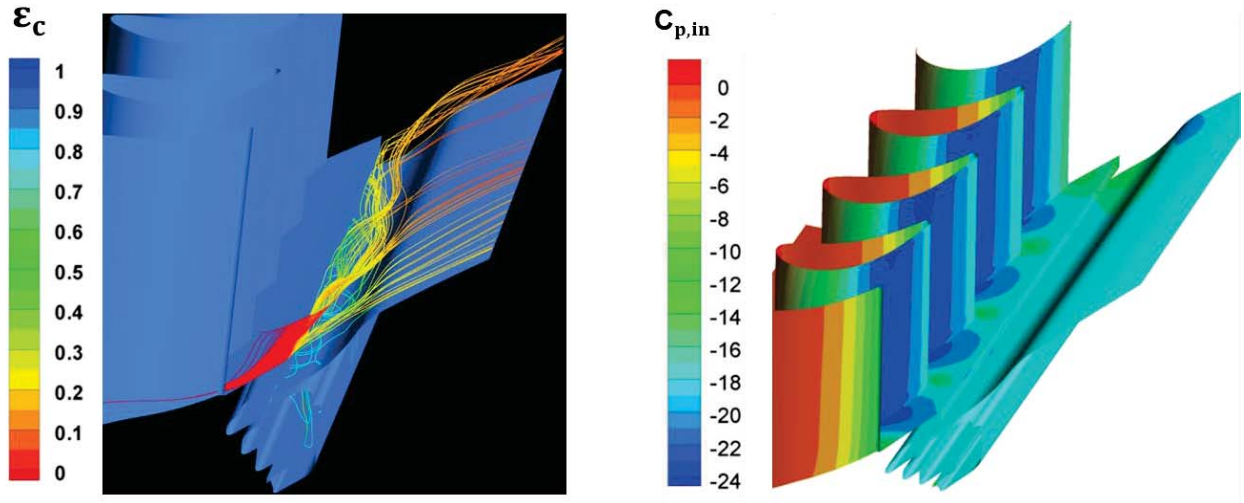

Figure 21: Streamlines and contours of pressure coefficient from the LSC five vane CFD simulations

Numerous CFD simulations were conducted to guide the modifications made to the LSC test section. The objectives of the CFD simulations were to ensure periodic flow in the region where the seal interfaces with the mainstream. Resulting from these simulations was the addition of a cross-flow loop in the seal exit region as shown in Figure 22. As can be seen from the illustrations, a flow loop containing a blower and a laminar flow element (LFE) was constructed and installed into the test section. The flow was introduced into the seal exit region at the outer vane location and the same flow was removed from the seal exit region at the inner vane location. The amount of cross-flow was determined through the CFD studies to meet the periodic objectives.

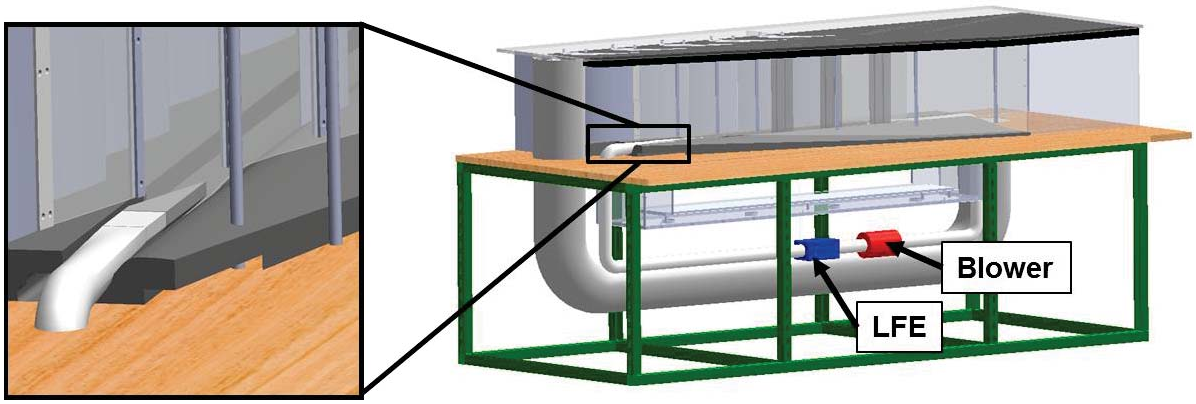

Figure 22. Overview of cross-flow loop with detail of cross-flow injection site

The effect of the cross-flow velocities induced by the flow loop can be seen in Figure 23 compared with the CFD solution of the infinite periodic cascade for a 0.5% purge flow rate from the seal. As the cross flow velocity ratio is increased from none (0.0) to 2.3, the static pressure coefficient more closely agrees with the CFD pressure coefficient for the periodic case. Note that the cross flow velocity ratio is defined as:

$$\gamma = \frac{V_\theta}{U_{in}}$$

The V_θ value is the mass-averaged velocity in the tangential direction whereas U_{in} is the vane inlet velocity. CFD simulations were conducted for each of the purge flows to determine the proper cross flow velocity ratio. The results of those simulations are shown in Table 2. It is interesting to note that as the purge flow increases, the cross flow velocity ratio decreases, which is expected given the strong purge flow influence. Comparisons of the CFD results were also made to the AFTRF in which the blades are rotating. The CFD predictions of the cross flow velocity ratio were found to be in good agreement with the AFTRF as shown in Table 3.

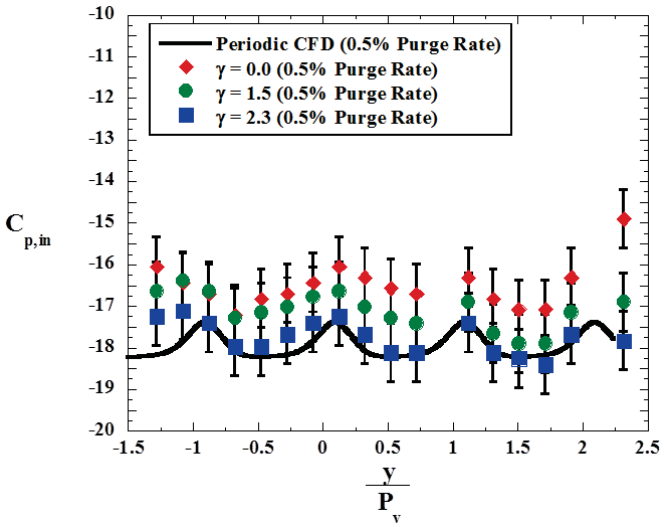

Figure 23. Variation of the vane endwall pressure distribution as a function of cross-flow rate

Table 2: Comparison of Optimal Cross-Flow Rates from the Periodic CFD and those from the LSC

Optimal Cross-Flow Velocity Ratio (γ)		
Purge Rate	**Periodic CFD**	**LSC**
0.5%	1.8	2.3
1.0%	1.1	1.2
1.5%	0.8	1.0

Table 3: Comparison of the Optimal Cross-Flow Rate from the LSC and that from the AFTRF

	LSC	**AFTRF**
Purge Rate	0.5%	0.5%
$\gamma = V_\theta/U_{in}$	1.8	1.7

As a comparison to the other purge flows, Figure 24 shows the measured platform static pressure variations for the cross flow velocity ratios that were determined through the CFD study. As can be seen by the data presented, the cross flow velocity ratios gave good periodicity along the endwall.

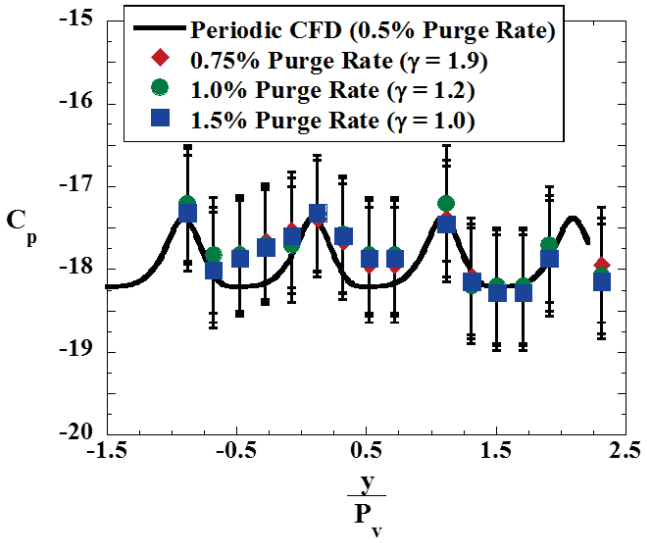

Figure 24. Vane endwall pressure distribution for various purge rates and cross flow rates

An uncertainty analysis was performed for sealing effectiveness, adiabatic effectiveness, and inlet pressure coefficient using the partial differential method described in Moffat (1985). The uncertainty of the reported inlet pressure coefficient values ranged from ±0.39 for a low value of 4.1 to ±0.71 for a high value of 17.4. Uncertainties in adiabatic endwall effectiveness were ±0.02 for both a low η value of 0.22 and for a high η value of 0.89. Sealing effectiveness was calculated with both thermocouples and carbon dioxide concentration sensing. For both methods, the uncertainties were dominated by the measurement of the temperature or carbon dioxide of the purge air in the plenum. Using the thermocouple method, uncertainties in sealing effectiveness were ±0.02 for a low ε_c value of 0.50 and a high value of 0.89. The carbon dioxide method yielded a similar uncertainty value, ±0.02 for values between ε_c = 0.5 and 0.8. Uncertainty of the purge flow rates were ±1% at the low value of 0.75% of the mainstream flow rate and ±0.5% at the high value of 1.5%. Error bars have been placed on figures where the uncertainty exceeds the size of the symbol.

Uncertainty for the flow field measurements was calculated using the perturbation method by Moffat (1985) due to the complex algorithms used to transform the non-orthogonal measurements in to an orthogonal coordinate system. Precision error was measured in the shear layer where the highest levels of turbulent kinetic energy were observed. This should provide an upper bound for the precision error. The uncertainty for the axial velocity, the tangential velocity, the radial velocity, and the turbulent kinetic energy were 5.25%, 0.95%, 20.1%, and 5.4% of their respective average values.

Sealing Effectiveness with and without the Downstream Bluff Body

Once the facility was properly modified to include the cross-flow loop, sealing effectiveness measurements were made for the various purge flow rates with the baseline seal geometry. The baseline geometry is shown in Figure 15. Sealing effectiveness measurements were made with thermocouple rakes whose pitchwise locations are shown in Figure 15. Each rake consisted of five thermocouples and spanned the entire seal exit. Uncertainty in sealing effectiveness was calculated to be ±0.02. Results for the various purge flows with the appropriately scaled cross-flow velocity ratios are shown in Figure 25. As would be expected, as the purge flow increases, the sealing effectiveness also increases.

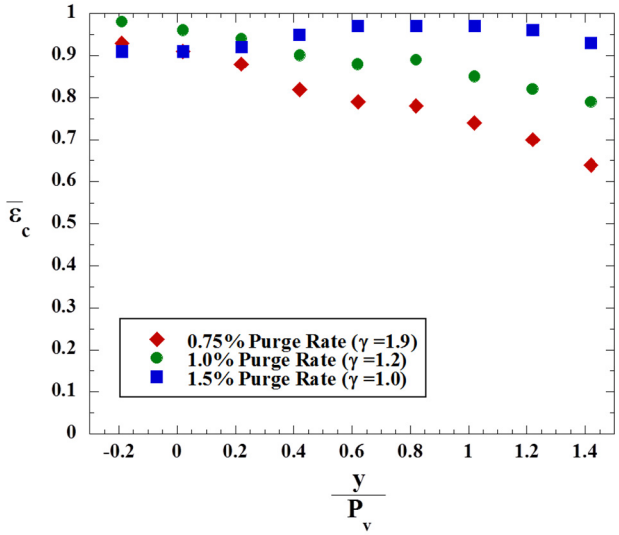

Figure 25. Rake-averaged sealing effectiveness at the rim seal exit with no bluff bodies present

One of the important questions being addressed in this study is to determine the effect of the downstream blade on the sealing effectiveness. As a result of this question, a bluff body was designed and constructed for the LSC experiments. The bluff bodies used are shown along with the endwall temperature contours in Figure 26 for the case with and without the bluff bodies. These temperatures contours give an indication of how quickly the coolant purged from the seal dissipates into the freestream. The contours also give an indication of the periodicity of the flow. The contours shown in Figure 26 illustrate the effect that the bluff bodies have on the endwall cooling pattern as compared to the case with no bluff bodies. In both cases the contours show a two-dimensional behavior in the cooling patterns. The results also show that as the purge flow rate is increased so is the cooling present on the endwall.

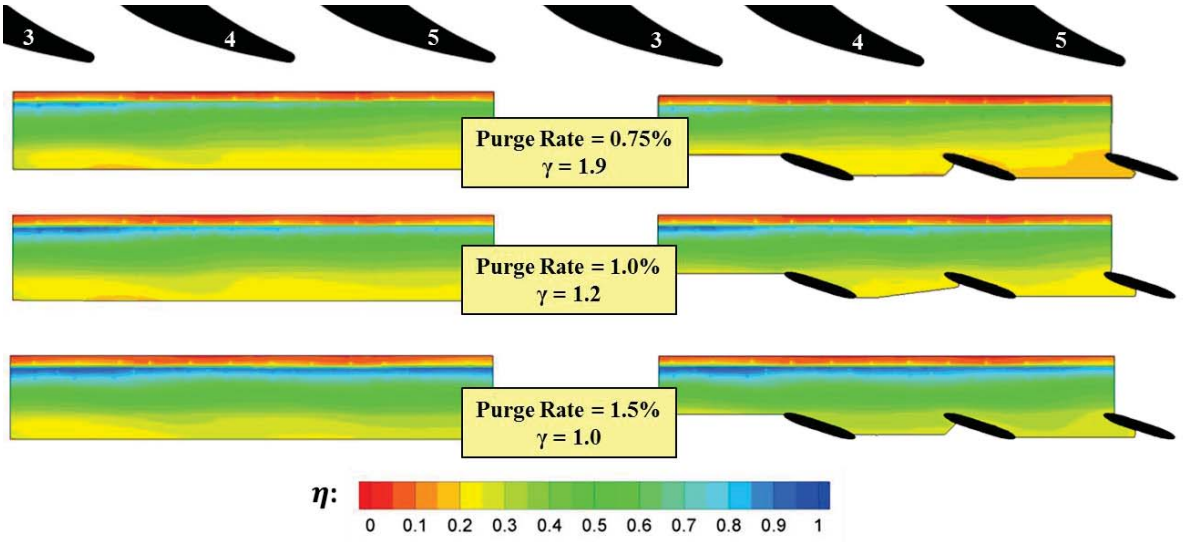

Figure 26. Comparison of endwall adiabatic effectiveness for the baseline rim seal with and without bluff bodies

The results in Figure 27 show the effect that the bluff bodies have on the overall sealing effectiveness for the various purge flows. The overall sealing effectiveness was calculated by averaging sealing effectiveness data from all of the thermocouple rakes into a single value. The bluff bodies decrease the overall sealing effectiveness. This effect is more pronounced for the lower purge flow rates. The largest decrease is approximately 10% overall sealing effectiveness. There was no effect of the bluff bodies in the case of 1.5% purge flowrate.

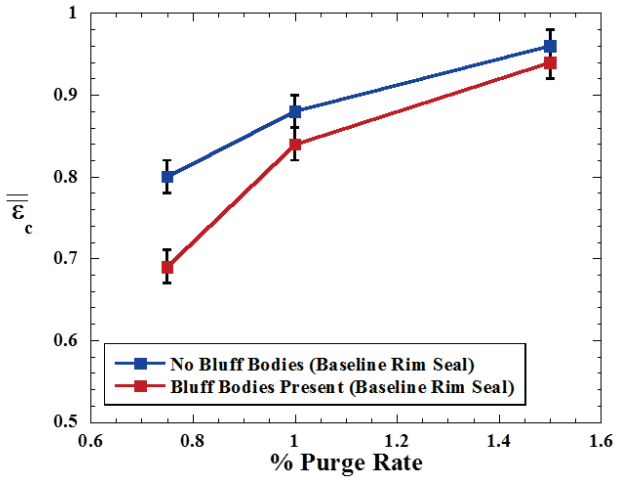

Figure 27. Pitch-average sealing effectiveness at the rim seal exit for the baseline rim seal with and without bluff bodies

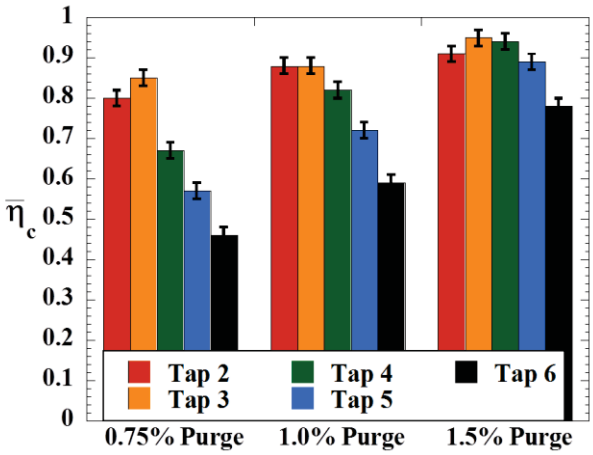

Figure 28. Nondimensional ingress levels throughout the baseline seal with bluff bodies present

Hot gas ingress levels were calculated using carbon dioxide (CO2) concentration measurements throughout the baseline seal, shown in Figure 28. The purge flow was seeded with 1% CO2 (based on molar concentration) and the seal flow was sampled through the ports labeled 2 through 6 in Figure 17. A nondimensional gas concentration was calculated as defined below:

$$\eta_c = \frac{\chi_c - \chi}{\chi_c - \chi_\infty}$$

An η_c value of 0 represents a high level of ingress where a value of 1signifies no ingress. Locations deep inside the seal (taps 2 and 3) showed consistently low levels of ingress. Locations near the trench (taps 4 through 6) showed the highest levels of ingress. As purge flow rate increased, the ingress near the trench decreased until all of the taps sampled yielded non dimensional gas concentration values higher than 0.7. The sensitivity of the region near the seal exit to increases in purge flow rate confirms that the instrumentation in the cascade is optimally placed to measure the impact of the main gas path pressure field on seal performance.

Effects of Bluff Body Clocking Position on Sealing Effectiveness and Adiabatic Endwall Effectiveness

An important question addressed by this work is that of what impact does the position of the downstream bluff bodies relative to the vanes have on rim seal performance. In an effort to answer this question, the location of the bluff bodies was shifted from their nominal clocking to two different alternate locations. The first was to the left by one third of the bluff body pitch. This location is referred to as the "+33% Clocking" position. The second location is one third of a bluff body pitch to the right of the nominal clocking location. This is referred to as the "-33% Clocking" location. These locations are shown in Figure 29.

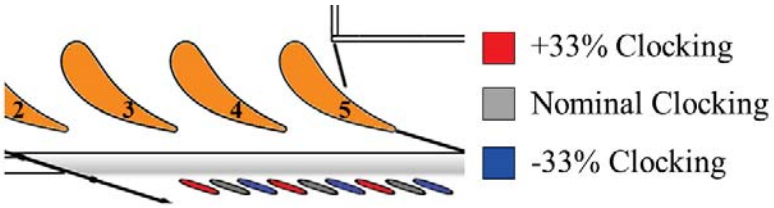

Figure 29. Bluff body positions for all three clocking locations considered

The different locations of the bluff bodies change how their pressure field interacts with that of the upstream vane row. This interaction can be seen in the mid-span pressure distributions around each bluff body, shown in Figure 30. The +33% Clocking position shows the most uniformity between the three bluff bodies. This variation in pressure is related to how the wakes of the upstream vanes impinge on each bluff body. This reduced level of variation in the "+33% Clocking" position indicates that at that position the bluff bodies are removed from the vanes wakes and encounter uniform freestream flow.

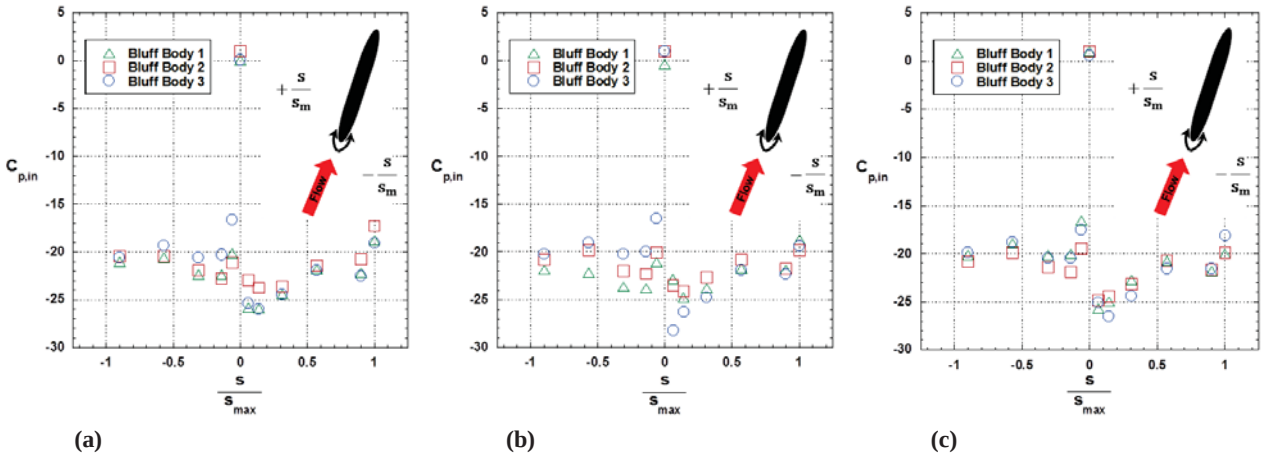

Figure 30. Pressure distribution from bluff body mid-span for the three clocking positions: (a) -33% pitch offset, (b) nominal position, (c) +33% pitch offset

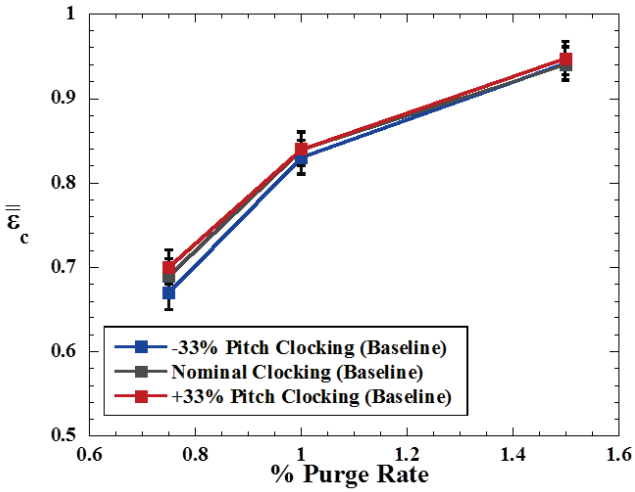

Figure 31: Effects of bluff body clocking on average sealing effectiveness for the baseline rim seal

Sealing effectiveness and adiabatic endwall effectiveness measurements were made to determine the effect of bluff body clocking on the baseline rim seal performance. Figure 31 shows the overall sealing effectiveness for the three clocking positions and at all three purge rates. The greatest variation occurs at the lowest purge rate. This is due to the rim seal becoming more insensitive to external influences with increasing purge rates. Even the greatest variation for the baseline rim seal, however, is still within or very near to the uncertainty of the measurement. The clocking position of the bluff bodies does not have a significant impact on the baseline rim seal.

Bluff body clocking effects on two different rim seals were studied. These two rim seals are diagramed in Figure 32. The first is the baseline rim seal. The second incorporated two endwall extensions. One of which was attached to the trailing edge of the vane endwall and the other to the leading edge of the blade endwall. This modification extends each endwall by 2.5% of the vane axial chord length. This rim seal modification is called the short combined extension or (SCE) and doubles the axial overlap of the rim seal exit.

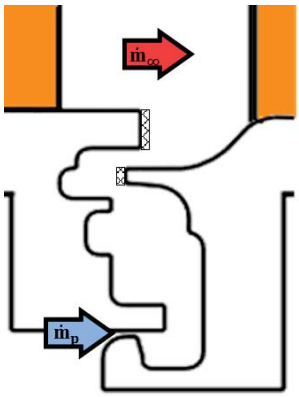

Figure 32: Schematic showing the baseline rim seal and the geometry changes included in rim seal modification SCE

Bluff body clocking position had a greater impact on the SCE than on the baseline rim seal. The overall sealing effectiveness for both rim seals is shown in Figure 33. The solid lines correspond to the data from the baseline rim seal while the dashed lines show the data from the modified rim seal. The trends between the two rim seals are similar. The -33% Pitch Clocking position shows the lowest sealing effectiveness while the +33 Pitch Clocking exhibited the highest. These trends are clearly more exaggerated for the modified rim seal. The trends however are near the uncertainty of the measurement. The location of the bluff body had minimal impact on overall sealing effectiveness for both the baseline and the modified seal.

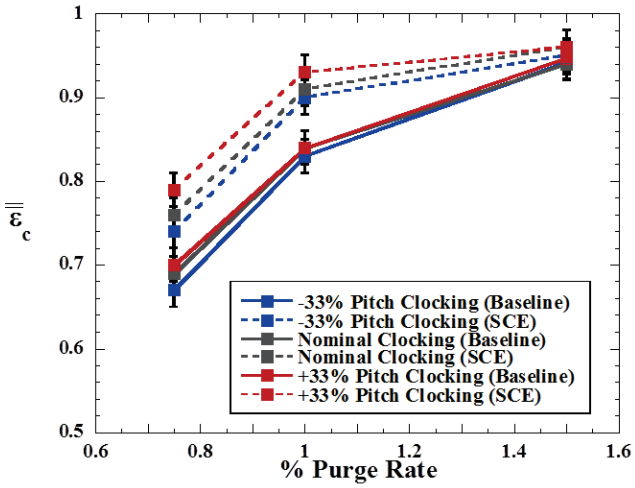

Figure 33: Average sealing effectiveness for the baseline rim seal and rim seal modification SCE with different bluff body clocking positions

The clocking effects on average sealing effectiveness at the lowest purge rate are better quantified in Figure 34. This figure shows the difference in average sealing effectiveness between the +33% Clocking and -33% Clocking positions from the nominal clocking position. The data from the nominal clocking position is denoted by the subscript "nom". For the baseline rim seal the difference is within the uncertainty of the measurement, which is 0.02. The difference is greater for the data from rim seal modification SCE. These data show a difference of 0.05 overall sealing effectiveness between the %33% and -33% clocking positions. While this difference is greater than the uncertainty of the measurement it is less than 10% of the value from the nominal clocking location.

The insensitivity of the baseline rim seal to bluff body position indicates that of the potential fields involved, that created by the vane row is dominant. This is supported by the increased variation in the data of the modified rim seal. By extending the vane endwall, the rim seal exit is moved away from the stronger regions of the vane potential field and closer to the potential field of the bluff bodies. This lessens the effect of the vane potential field and increases that of the bluff bodies on the rim seal.

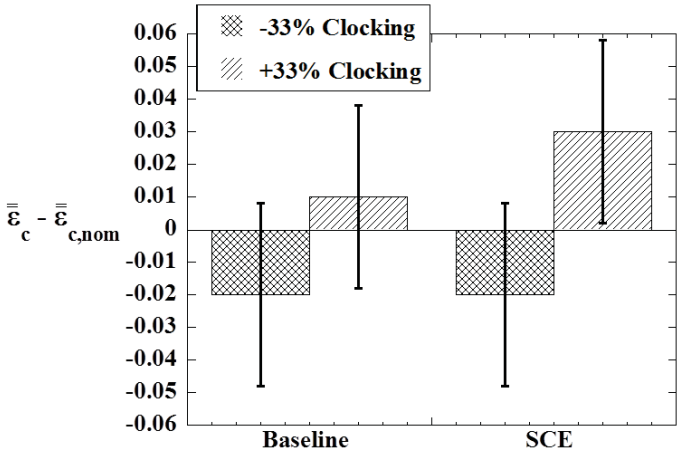

Figure 34: Effects of bluff body clocking on average sealing effectiveness for the baseline rim seal and rim seal modification SCE (0.75% purge rate)

It is desired that through modification of the rim seal geometry that pitch-average sealing effectiveness may be increased. This augmentation in sealing effectiveness was evaluated at the rim seal exit for both rim seals. Bluff body clocking position was observed to have an impact on this augmentation. Figure 35 shows the augmentation in pitch-average sealing effectiveness due to rim seal modification SCE. The subscript 0 denotes data from the baseline rim seal. All three clocking positions and all three purges are shown. For the lower purge rates, 0.75% and 1% of the mainstream, an increase of 0.06 to 0.09 was observed respectively. The highest purge rate, 1.5% of the mainstream, indicates no definite improvement. This is due to the fact that the baseline rim seal was already highly purged at this purge rate. The data from the purge rates where definite improvement in pitch-average sealing effectiveness was observed indicate that the +33% Pitch Clocking position tended to show slightly higher improvements. Bluff body clocking effects are smaller than the augmentation due to the rim seal modification considered.

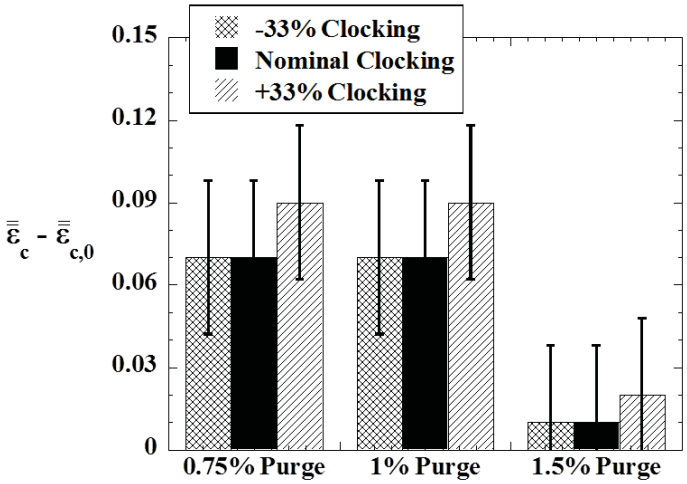

Figure 35: Increase in average sealing effectiveness due to rim seal modification SCE for various bluff body clockings and purge rates

The effect of bluff body clocking position on adiabatic endwall effectiveness was also considered. Adiabatic endwall effectiveness, defined below, was calculated from IR thermography measurements of the endwall temperature. Adiabatic endwall effectiveness values were averaged over the area outlined in red in Figure 15 to produce a metric to compare various seal geometries. Average adiabatic endwall effectiveness values for all rim seals, bluff body positions, and purge rates are shown in Figure 36. Uncertainty in adiabatic endwall effectiveness was calculated to be ±0.02. Bluff body clocking position shows little effect on the average endwall effectiveness. This indicates that the mixing in the trench is not greatly affected by bluff body clocking.

$$\eta = \frac{T_\infty - T_{aw}}{T_\infty - T_c}$$

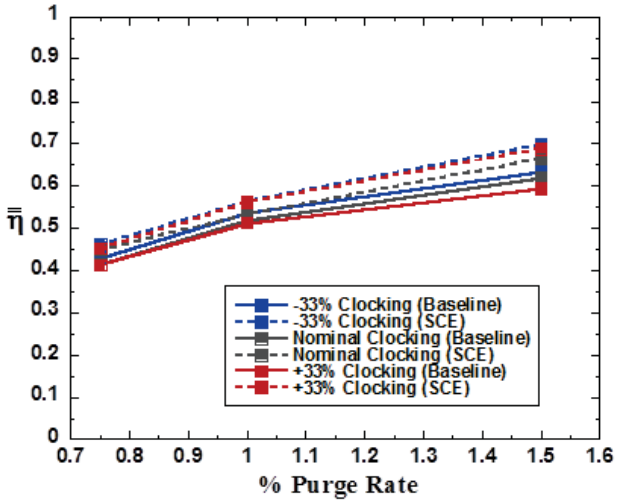

Figure 36: Effects of bluff body clocking on average endwall adiabatic effectiveness for the baseline rim seal and rim seal modification SCE

Trends in adiabatic endwall effectiveness augmentation due to rim seal modification were consistent with those from the sealing effectiveness data. This augmentation is shown in Figure 37 for all clocking positions and purge rates. The "+33% Clocking" position consistently showed the highest increase. The augmentation at the "-33% Clocking" position was comparable to or less than that at the nominal clocking.

Bluff body clocking position was varied by 33% of the bluff body pitch to either side of the nominal position. The effect of this variation on average sealing effectiveness at the rim seal exit and average adiabatic endwall effectiveness was studied. The variations in seal performance and adiabatic endwall effectiveness due to bluff body position were small. The insensitivity of the seal flow to bluff body position is mostly like due to the relatively small horse shoe vortex at the leading edge of the bluff body. The interaction between the seal flow and the horse shoe vortex at the leading edge of a blade has been shown in the literature to be sensitive to blade position. The bluff body was designed to match the pressure distortion of a rotating blade in a stationary reference frame. The leading edge radius of the bluff body is therefore much smaller than that of the blade, resulting in a smaller horse shoe vortex. The smaller vortex is not nearly as sensitive to bluff body position.

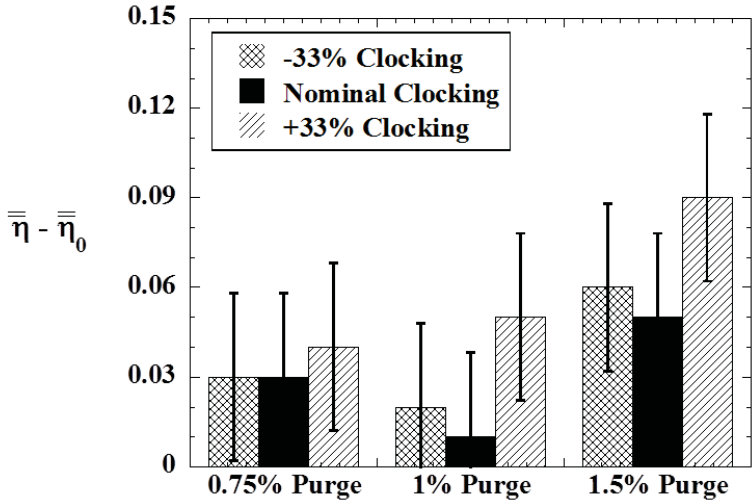

Figure 37: Effects of bluff body clocking on the increase in average endwall adiabatic effectiveness due to rim seal modification SCE

Parametric Study of the Rim Seal Geometry

To better understand the trends associated with various rim seal geometry components, a parametric study of rim seal geometry was carried out. The effect of the axial overlap at the rim seal exit was the main focus of the study. Figure 38 shows the three rim seal modifications included in the study. The first modification consists of extending the blade endwall leading edge. The second represents an extension of the vane endwall trailing edge. The third modification is the combination of the first two.

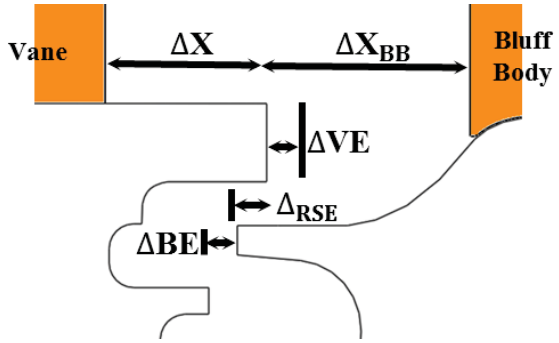

Figure 38: The relative location of the seal and the locations of the endwall extensions used in the parametric study on seal geometry.

Table 4: Baseline Seal and Modification Parameters

	$\Delta X/C_{ax}$	$\Delta X_{BB}/C_{ax}$
Baseline	0.24	0.30
Seal Modification	$\Delta VE/\Delta_{RSE}$	$\Delta BE/\Delta_{RSE}$
Baseline	-	-
Short Vane Endwall Ext. (SVE)	0.55	-
Long Vane Endwall Ext. (LVE)	1.66	-
Short Blade Endwall Ext. (SBE)	-	0.55
Long Blade Endwall Ext. (LBE)	-	1.66
Short Combined Ext. (SCE)	0.55	0.55
Long Combined Ext. (LCE)	1.66	1.66

Two different sizes of each rim seal modification were considered in the study and are listed in Table 4. The small combined extension increases the axial overlap at the rim seal exit by 110%. The larger combined extension increases the axial overlap by 330%. Thus the naming convention for the rim seal modifications consists of the short and long blade endwall extension (the S.B.E. and L.D.E. respectively), the short and long vane endwall extension (the S.V.E. and L.V.E. respectively) and the short and long combined extension (the S.C.E. and L.C.E. respectively).

Extending the blade endwall serves to alter the axial momentum of the coolant in the seal. Due to the horizontal orientation of the rim seal exit, coolant with higher axial momentum will more effectively prevent the ingestion of main gas path fluid. The baseline rim seal and modification SCE have the minimum area of the seal in the vertical direction. Thus the coolant travels up and impinges on the underside of the vane endwall trailing edge in the vicinity of the rim seal exit. Impingement of coolant results in lower axial momentum as it mixes with gas from the trench at the rim seal exit. Increasing the blade endwall length directs the coolant into a hairpin turn preceded and followed by stretches of horizontal pathways before it reaches the rim seal exit. This increases the axial momentum of the coolant stream at the rim seal exit. Extending the vane endwall removes the source of ingested fluid from the rim seal. By extending the vane platform trailing edge the rim seal exit is distanced from the potential field of the vane which was earlier noticed to be the dominant in the ingestion process. Additionally, extending the vane endwall decreases the width of the trench through which ingress may occur.

Extending the vane and blade endwall alters the flow patterns in the rim seal as well as the trench. The effects of these changes on pitch-average sealing effectiveness are illustrated in Figure 39 The data from the largest rim seal modifications are shown as they display the observed trends most clearly. The largest extension of the blade endwall, rim seal modification LBE, yields negligible sealing effectiveness gains over the baseline rim seal. This indicates that the influence of the trench flow field at the rim seal exit dominates the increase in axial momentum of the coolant.

Significant gains were observed when the vane endwall was extended. This increase in sealing effectiveness arises from the effect of the vane potential field on the seal being mitigated and the decrease in axial width of the trench. Most interesting was the observation of a further increase in sealing effectiveness when the bluff body and vane endwalls were extended simultaneously (compare the LCE and LVE). This deviates from the negligible impact rim seal modification LBE had alone. The increase in axial coolant momentum caused by the blade endwall extension may have a positive impact on sealing effectiveness at the rim seal exit when extending the vane endwall weakens the influence of vane row.

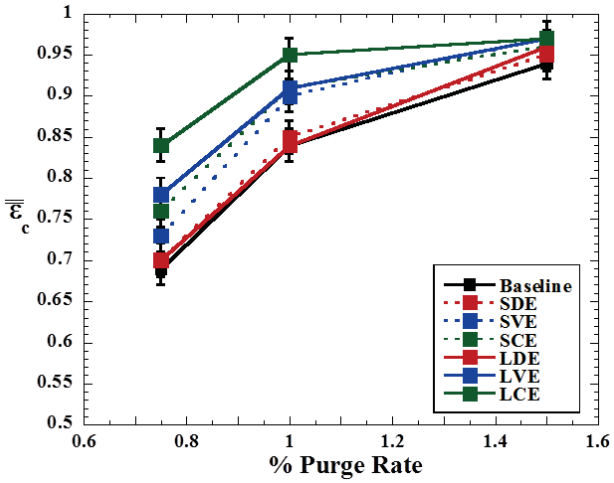

Figure 39: Average sealing effectiveness at the rim seal exit for rim seal modifications LBE, LVE, and LCE

The effect of each seal modification on sealing effectiveness is shown in Figure 40. The trends in the short extensions are similar to those of the long extensions previously discussed above. Those trends are most pronounced at the lowest purge rate (0.75% of the mainstream flow). As the purge rate decreases, seal design plays are larger role in preventing ingress.

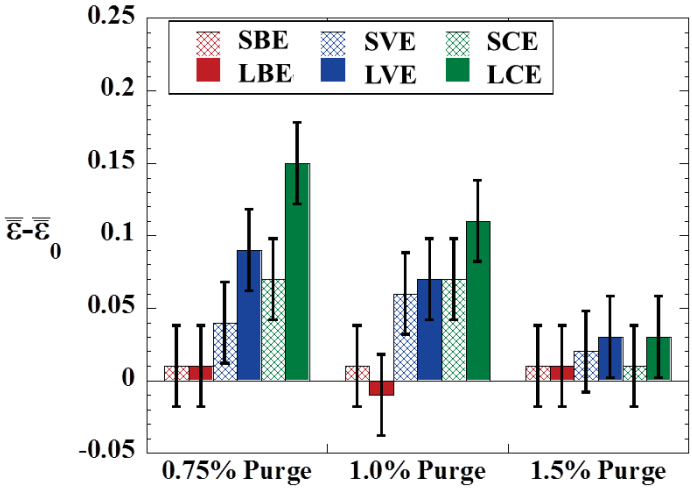

Figure 40: Improvement in sealing effectiveness relative to the baseline seal for all seal geometry modifications

The effect of rim seal modification on adiabatic endwall effectiveness was also considered. Figure 41 shows the effect of modification size on endwall effectiveness. The smaller modification showed only modest increase over the baseline rim seal. However by tripling the size of the endwall extensions, the average adiabatic effectiveness rose significantly. Figure 42 confirms that the largest seal extensions yielded the largest increases in endwall effectiveness. By increasing the vane endwall extension from 2% vane axial chord to 6%, the average endwall effectiveness increases by a factor of 2 to 4 depending on purge rate and rim seal modification. Only at the highest purge rate did the short vane and combined endwall extensions (the SVE and SCE respectively) modestly increase cooling on the endwall. At the lower purge rates, the increase in endwall effectiveness was very near the uncertainty of the measurement (0.02 overall effectiveness).

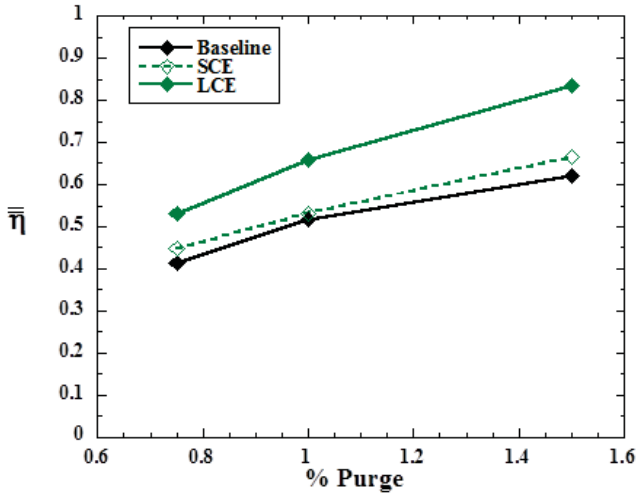

Figure 41: Average endwall adiabatic effectiveness for rim seal modifications SCE and LCE

Figure 42 also shows that the cooling of the blade endwall was most affected by extending the vane endwall. The long vane endwall extension (the LVE) shows a considerable large increase than the long blade endwall extension (the LBE). Extending the vane endwall decreases the amount of ingress into the trench. As a result, the purge flow has a larger impact on the endwall temperatures. The long combined endwall extension (the LCE) yields even higher endwall effectiveness levels than the LVE. The higher momentum purge flow is reaching farther out into trench before mixing with the trench flow.

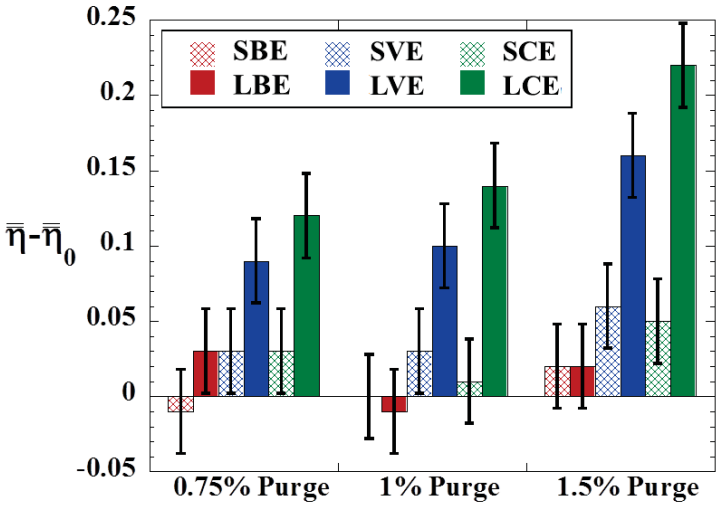

Figure 42: Increases in average endwall adiabatic effectiveness for all rim seal modifications and all purge rates

A parametric study of the axial overlap at the exit of a radial overlap rim seal illustrates the relationships between the various endwall extensions and the performance of the rim seal.

Increasing the axial overlap by extending the blade endwall alone had minimal effect on the average sealing effectiveness at the rim seal exit and average adiabatic endwall effectiveness in the trench. Increasing the axial overlap by extending the vane endwall showed increased sealing and adiabatic effectiveness. Adiabatic effectiveness showed the greatest improvements when the largest vane endwall extension was used. The greatest gains in sealing and adiabatic effectiveness were obtained by simultaneously extending the vane and blade endwalls simultaneously.

Flow field measurements in the trench region of the rim seal

Flow field measurements in the trench region of the seal were made to illustrate the mechanisms behind the trends in seal performance previously reported. A key goal is to understand the mechanism through which hot gas from the main gas path enters the trench and then ingresses into the seal. Measurements of the three component velocity field were made using Laser Doppler Velocimetry. Measurements were made at two pitchwise locations in the trench, identified in Figure 43a. The first plane was located at the mid-pitch locations between the trailing edges of Vanes 3 and 4 and will be hereafter referred to as the mid-pitch plane. The mid-pitch plane coincides with an area of low endwall pressure as demonstrated in Figure 24. The second plane was placed in a region of high endwall pressure behind the trailing edge of Vane 4. The second plane was labelled as the vane trailing edge plane. Each plane covered axial and radial dimensions shown in Figure 43b. The locations of the two measurement planes facilitate the study of the changes in the trench flow field due to the passing of the vane wake. The wake of vane 3 had yet to cross the trench at the mid-pitch plane. The vane trailing edge plane corresponds to the location where the wake from vane 3 has nearly completely traversed the trench.

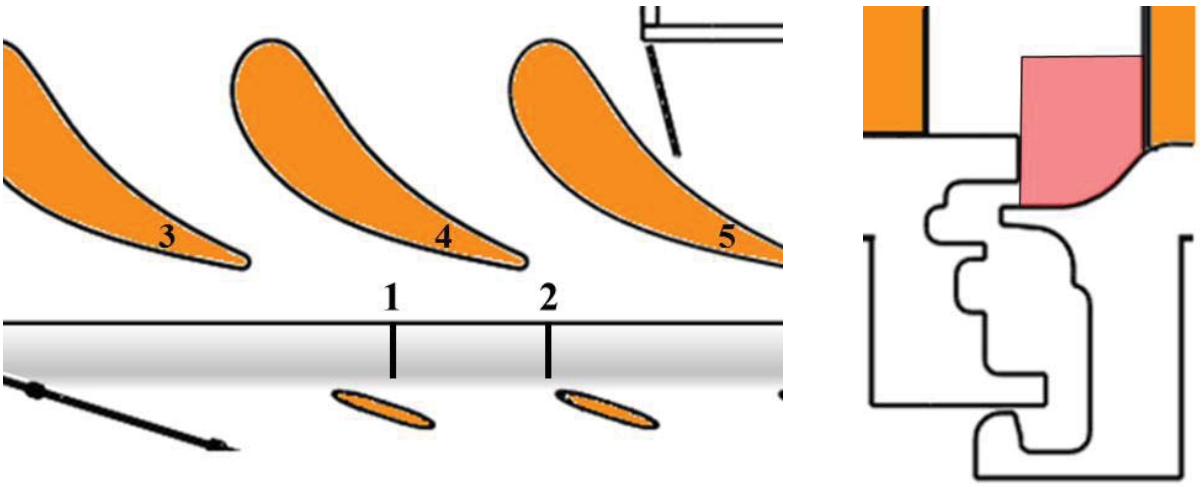

(a) **(b)**

Figure 43: Description of the planes over which flow field data were taken with the (a) pitchwise locations and (b) the radial and axial dimensions.

The flow fields at the mid-pitch and vane trailing edge planes are shown in Figure 44a and Figure 44b respectively. Vectors of in-plane velocity are shown with contours of pitchwise velocity normalized by the cascade inlet velocity. The quality of the data is supported by the good agreement between the normalized velocity in the main gas path (approximately four) and

the area ratio of the vanes in the cascade. The flow in the trench is predominately in the pitchwise direction due to the large amount of turning of the vanes. The purge flow was introduced into the seal with little pitchwise momentum. As a result, the regions of lowest pitchwise velocity in Figure 44 are close to the seal exit. Therefore fluid in areas of high pitchwise momentum must come from the main gas path.

The flow at the mid-pitch plane, Figure 44a shows flow traveling along the blade endwall towards the rim seal exit. Partial ingress of the trench flow is observed at the seal exit. The fluid that does not enter the seal exit is turned up the vane endwall trailing edge by the purge flow. A shear layer is observed at the interface between the main gas path and the trench flow but does not extend more than three percent of the vane exit span into the main gas path. Figure 44b shows a distinctly different flow field at the vane trailing edge plane. Notably, the shear layer observed at the mid-pitch plane is replaced by a large region of low momentum fluid in front of the bluff body leading edge. The contours shown in Figure 45 indicate that removing the bluff body significantly decreases the low momentum fluid in the main gas path. This region of low momentum fluid extends more than ten percent of the vane exit span. The presence of low momentum fluid in the main gas path has a negative impact on aerodynamic efficiency. Fluid from the main gas path is also drawn into the trench at the trailing edge of the vane endwall due to the relatively high pressure at the vane trailing edge.

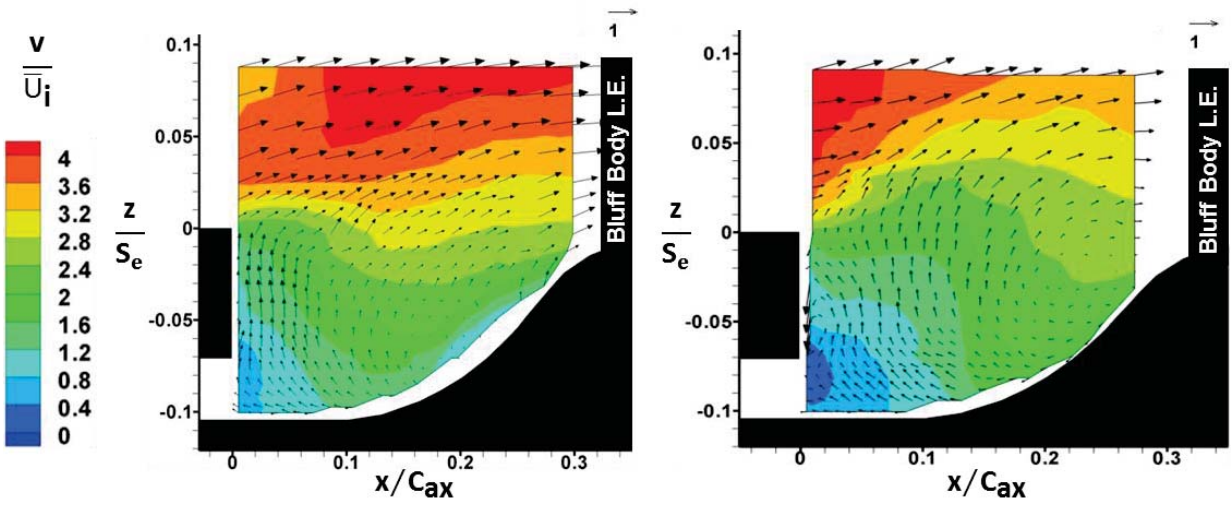

Figure 44: Contours of normalized pitchwise velocity with in-plane vectors for the baseline seal at (a) the mid-pitch plane and (b) the vane platform trailing edge plane.

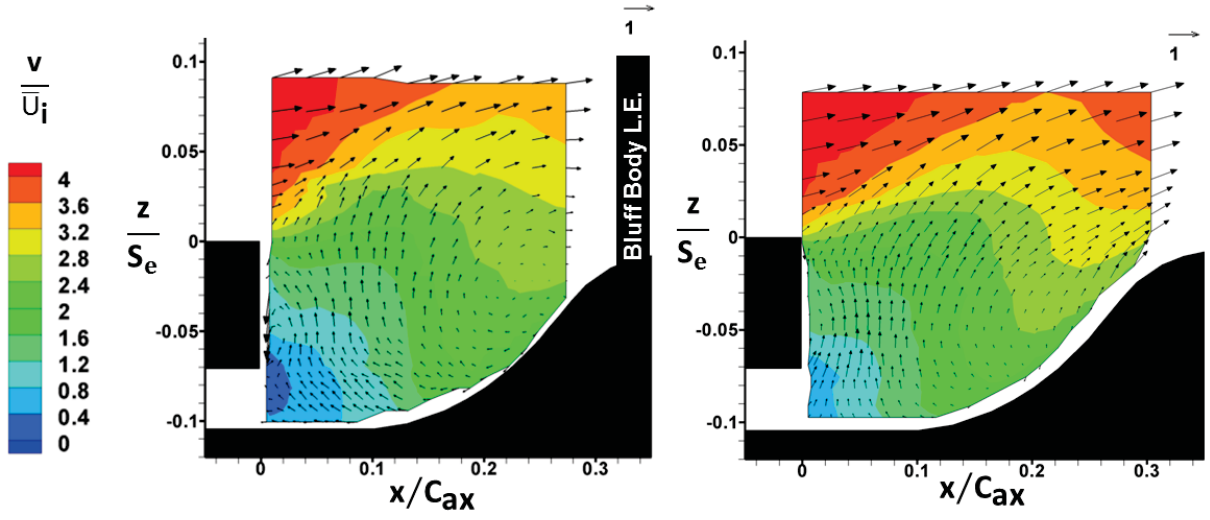

Figure 45: Contours of normalized pitchwise velocity with in-plane vectors for the vane trailing edge plane for the baseline seal (a) with the bluff body and (b) without the bluff body.

Turbulence plays an important transport role in the trench. Levels of turbulent kinetic energy (TKE) are shown in Figure 46. High levels of TKE are observed where the trench flow interfaces with the main gas path. Turbulence is produced in regions of gradients in mean velocity resulting in the highest levels of TKE. The unsteadiness of the enwall flows from the upstream vane further increases TKE in this region. Turbulence is transported throughout the entire trench region. Profiles of TKE in the trench shown in Figure 47 indicate that turbulence in the trench is as much as an order of magnitude larger than levels in the main gas path. Turbulence intensity levels were between 25 and 75 percent of the local velocity. The higher levels occurred near the seal exit due to the lower velocity associated with the purge flow. The significant turbulent mixing accounts for the low gradients of endwall adiabatic effectiveness shown in Figure 26. Turbulence mixes hot gas from the main gas path with the purge flow. The resulting mixture is then transported through the seal exit as indicated by the vectors in Figure 44.

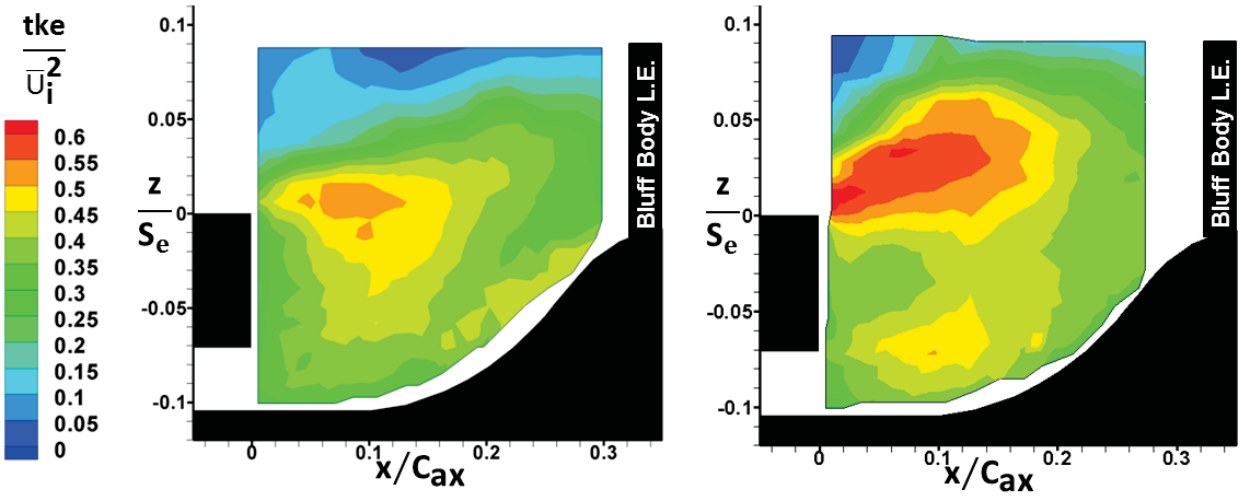

Figure 46: Contours of normalized turbulent kinetic energy for the baseline seal at (a) the mid-pitch plane and (b) the vane platform trailing edge plane.

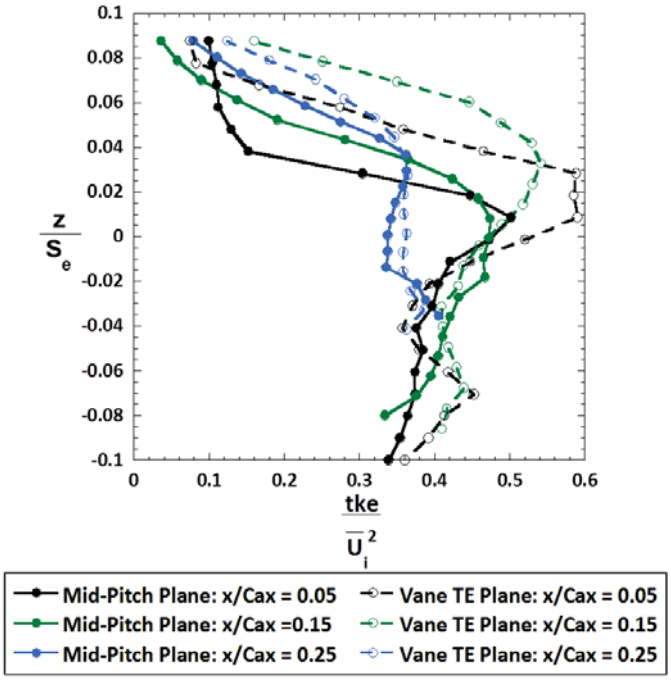

Figure 47: Profiles of turbulent kinetic energy from the baseline seal

A parametric study of the axial overlap at the seal exit was used to identify the effect of seal geometry modification on the transport mechanisms of hot gas ingress. Flow field measurements were made for the baseline seal as well as the LCE and LVE modifications. As the trends between the LCE and the LVE are similar, data from the LCE are compared with those from the baseline seal. The mean flow fields for the trailing edge plane of the baseline and LCE are shown in Figure 48. Extending the vane endwall reduced the tangential momentum of the fluid in the trench. The diminished effect of the vane pressure field and the decreased size of the trench width prevented hot gas from being drawn into the trench as observed with the baseline seal. Low momentum fluid is still pulled out into the mainstream.

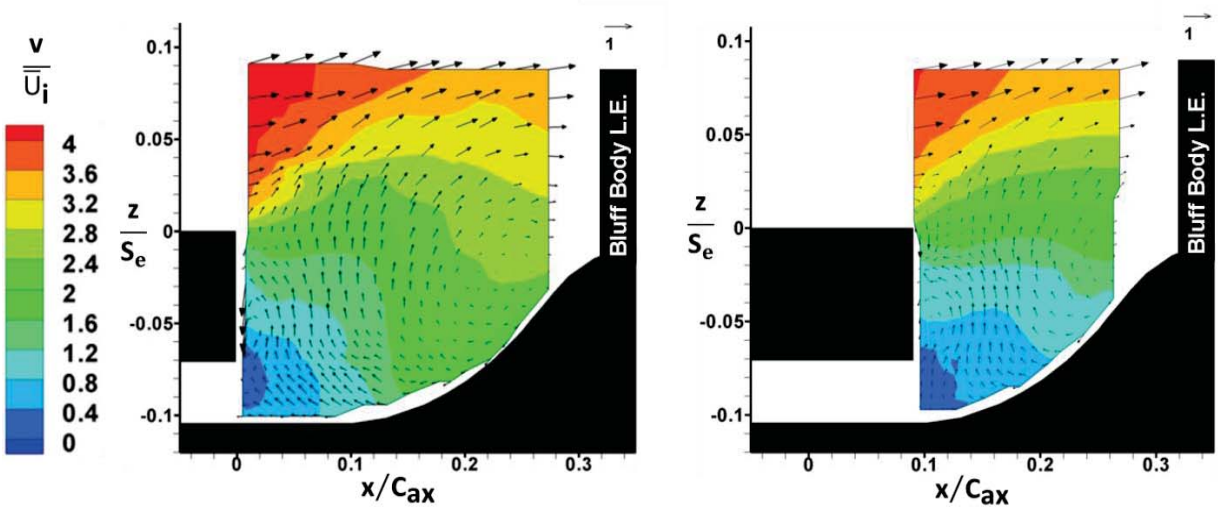

Figure 48: Contours of normalized pitchwise velocity from the vane trailing edge plane of the (a) baseline seal and (b) the L.C.E. seal.

Extending the vane endwall also altered the turbulence in the trench flow field. Contours of TKE are shown in Figure 49 for the baseline seal as well as the LCE. The location of peak turbulence in for the LCE is shifted to the back of the trench. Extending the vane endwall altered the trajectory of the vane endwall flows. The unsteadiness of these flows may account for the high TKE levels near the bluff body leading edge. The turbulence near the seal exit in the LCE was diminished relative to the baseline seal. The profiles of TKE shown in Figure 50 indicate that the turbulence levels are somewhat comparable between the two seals. The gain in seal performance observed in the LCE and the LVE is due to the decrease in fluid being drawn into the trench as the vane wake crosses the trench and not due to diminished turbulent mixing.

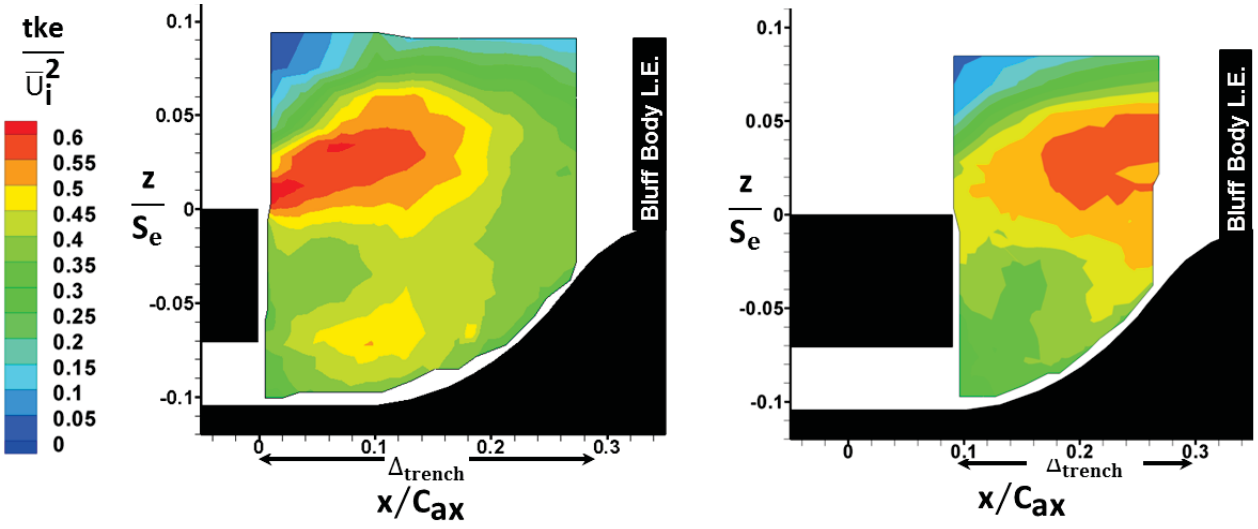

Figure 49: Contours of normalized turbulent kinetic energy from the vane trailing edge plane of the (a) baseline seal and (b) the L.C.E. seal.

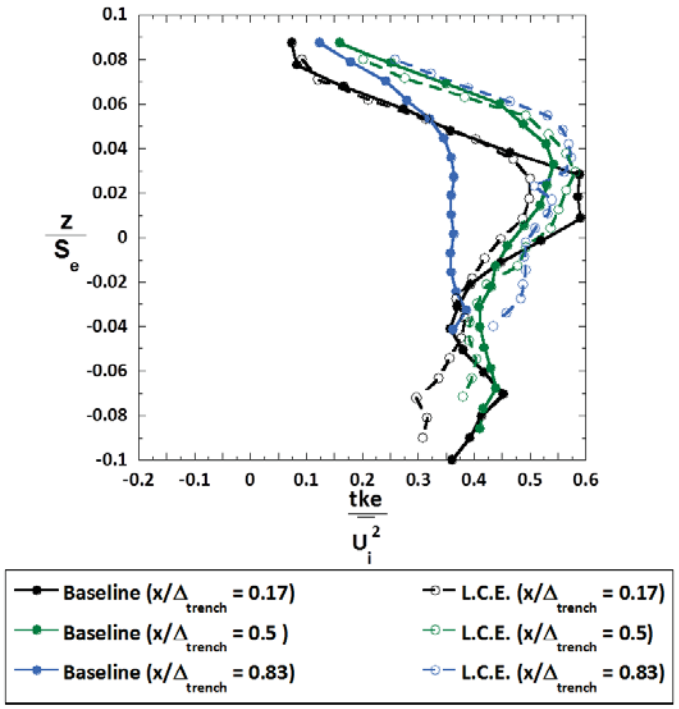

Figure 50: Profiles radial velocity from the vane trailing edge plane of the baseline and L.C.E. seal.

A cascade was used to study the effect of the main gas path pressure field on rim seal flows. The pressure field of both an upstream vane and a downstream blade were included in the study. The unsteady pressure field of a downstream blade was modelled using a bluff body. Bluff body clocking position had little effect on sealing effectiveness and adiabatic endwall effectiveness. The bluff bodies captured the pressure field of the blade but exhibited much smaller endwall flows than would exist in front of a rotating blade. The blade endwall flows have been shown to vary in size and interact with rim seal flows based on blade clocking position. The diminished endwall flows in front of the bluff bodies were too small to impact the flow in the trench region of the seal.

A parametric study of seal geometry studied the impact of the axial overlap at the seal exit on seal performance. Extensions on the vane endwall, the blade endwall, and both endwalls simultaneously were used in the study. Extending the vane endwall increased sealing effectiveness as well as endwall cooling more than the extension of the blade endwall. The main mechanisms behind these improvements were the diminished impact of the vane pressure field and the decrease in trench width. A slight trend was observed that extending both endwalls simultaneously performed better than extending either alone.

Flow field measurements in the trench region of the seal were made using a 3-component LDV system. Keys features of the trench flow field include recirculation pockets downstream of the vane trailing edge. A significant shear layer was observed varying in height between 5% and 10% vane exit span. Low momentum fluid was observed to build up in front of the bluff body. Significant levels of turbulence kinetic energy were observed in the trench of all of the seals studied. The turbulence in the trench was enhanced by the unsteadiness of the vane endwall flows passing overhead of the trench. Extending the vane endwall altered the path of the vane endwall flows resulting in the peak TKE of the LCE to be located at the back of the trench.

3 AFTRF Rotating Rig

Detailed descriptions of the overall facility, instrumentation configuration, and testing methods can be found in the Appendix section of this report. A brief summary will be provided here. The AFTRF facility had a pre-existing vane, blade, and rim cavity installed that were replaced with P&W hardware for the purposes of this NRA contract. Existing rig instrumentation ports, flow supplies, and measurement windows were re-used for the current work. Further hardware modifications to the AFTRF rig consisted of the alteration and installation of a purge chamber that was used to introduce purge fluid into the rim cavity. Modifications were made to a chamber that had been built for a previous DOE sponsored research program. The current leakage flow system is driven from a high pressure (300 psi) air reservoir. Up to 1.5% leakage flow mass flow rate is available in the current arrangement. The mass flow rate is monitored by a calibrated ASME orifice. Figure 51shows a photo of the AFTRF after the new P&W hardware was installed.

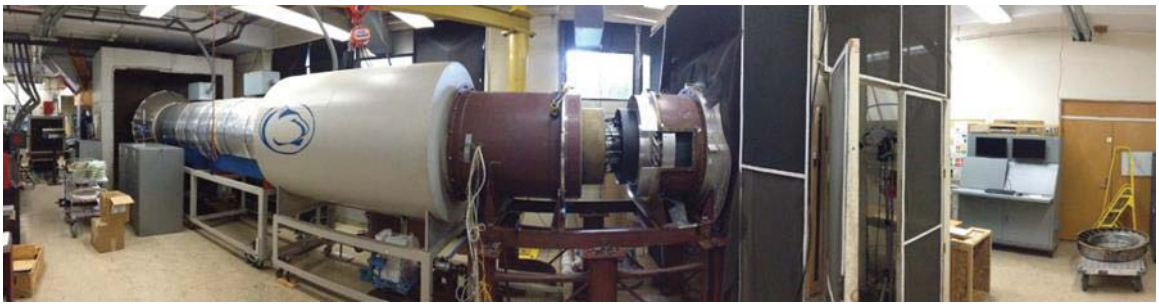

Figure 51: AFTRF Facility With P&W Hardware For NRA Testing

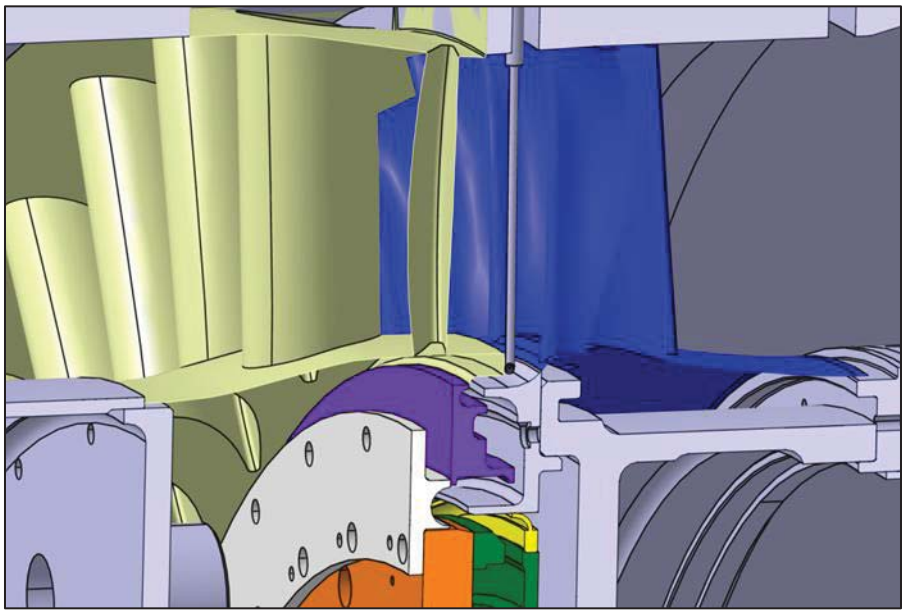

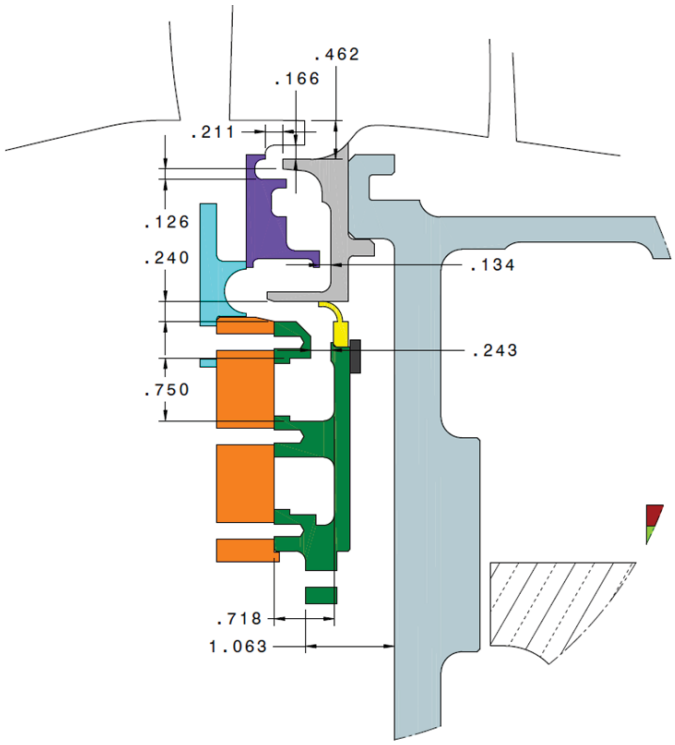

Figure 52: AFTRF Purge Chamber (green and orange components)
Inserted Below the Rim Cavity Region (purple and grey components)

A cross section of the purge flow chamber and rim-cavity seal exit are shown in Figure 52. A non-rotating, flexible rubber seal was installed on the purge chamber to prevent leakage fluid from exiting the cavity before entering the main gas path flow. This rubber seal is represented in Figure 52 as the yellow component. A photograph of the installed hardware is on the left in Figure 53. The outer radius of the seal rubs against the rotating side of the rim cavity (gray component in cross section).

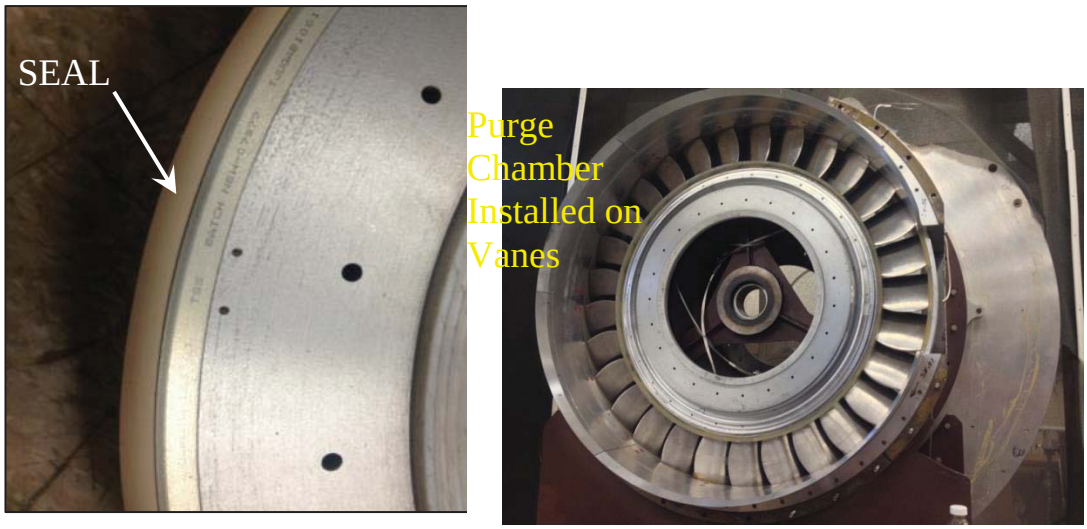

Figure 53: AFTRF Purge Chamber with the Seal Attached

AFTRF Instrumentation

The AFTRF started to generate baseline data in November 2012 after hardware delivery to the laboratory was completed. Below is a summary of the installed measurement capability/systems:

- NGV inlet flow traverse system
- AFTRF Facility measurement control system and its computer/data interface
- 150 channel slip-ring based data transmission system
- NGV exit computerized flow traverse system
- Rotor phase-locked measurement system
- A Kiel probe based local total pressure measurement system
- A five hole probe calibration jet for AFTRF class measurements
- A time accurate total pressure measurement probe using a 150 Khz Endevco sensor (including its optical encoder based data collection/processing system)
- Time accurate static pressure measurements using a 150 Khz Endevco sensors in the rim-cavity

A detailed view of the inlet measurement pitot probe is shown in Figure 54. The circumferential locations of the inlet probes are shown on the left and a picture of an inlet probe is on the right. During testing, the pneumatic average of the three probes was used to determine the inlet total pressure to the rig.

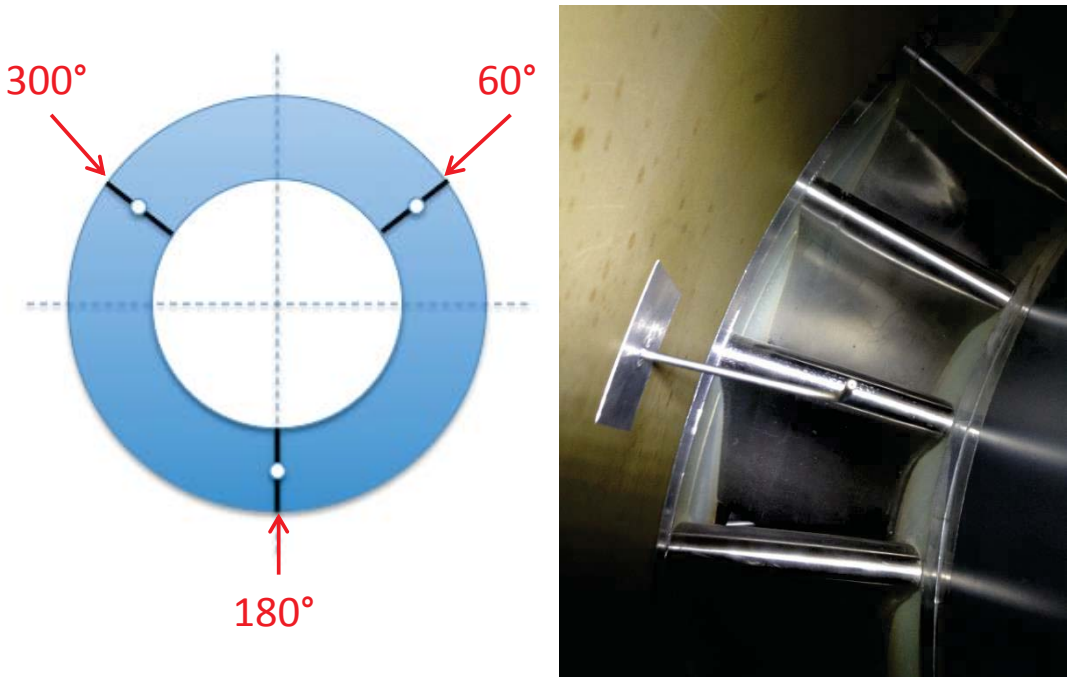

Figure 54: AFTRF Inlet Measurement Section (mid-span and full span traverses at one chord upstream of the NGV)

Three of the inlet vanes were each instrumented with surface static pressure taps at three spanwise locations: 10%, 50%, and 90%. Surface static pressure measurements were also available on two of the rotor airfoils. These radial positions were 10%, 25%, 50%, 75%, and 90%.

Figure 55 shows a close-up of the purge exit region. Shown at this location is the insertion of a sub-miniature Kiel probe for the detailed measurement of vane exit quantities. The circumferential extent of these exit traverse planes was one vane pitch. Radial extents were between 10% to 90% span. A five-hole probe was also used to obtain flow exit angles and velocities.

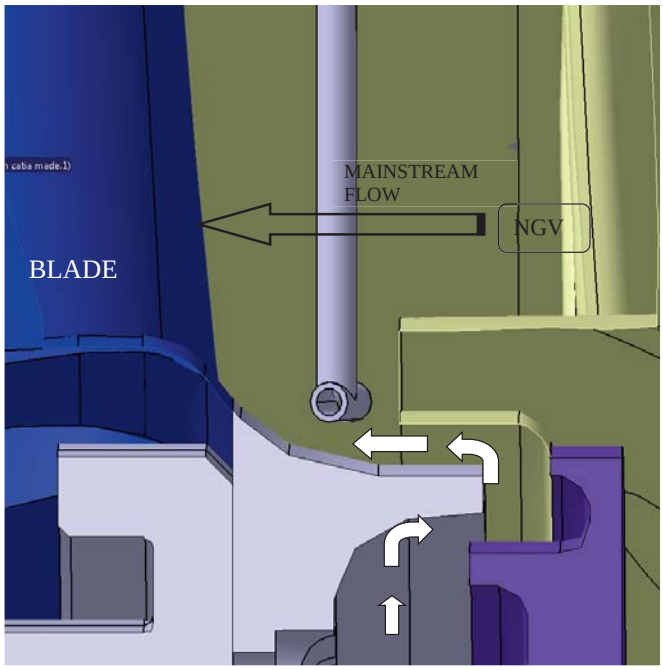

Figure 55: Exit area of the purge chamber

The AFTRF rotor also houses a rotating probe traversing mechanism, in addition to a 32 channel electronic pressure scanner. Connections to a 150 channel slip-ring system were re-designed and re-assembled to achieve a higher system reliability and ease of dis-assembly. This instrumentation is shown in Figure 56.

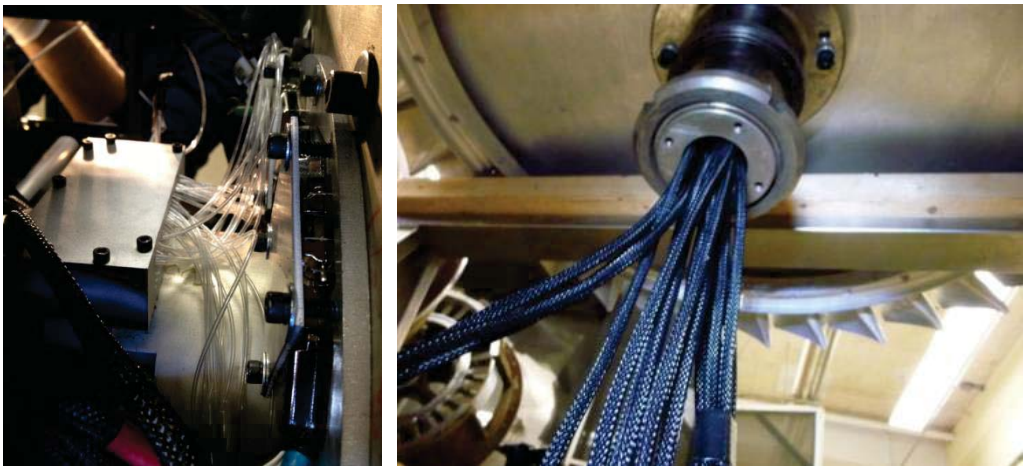

Figure 56: AFTRF Slip-Ring Instrumentation.

A rotating probe traversing mechanism that can move an aero/thermal probe in both radial and circumferential directions was operated in AFTRF in Spring 2013. This traverser system allows a "high measurement grid resolution" for rotating frame measurements. A schematic of this measurement system is shown in Figure 57. Although much effort was given to the installation of this measurement system, useful data was never recorded and the program made the decision to forgo this measurement so that more geometries could be tested.

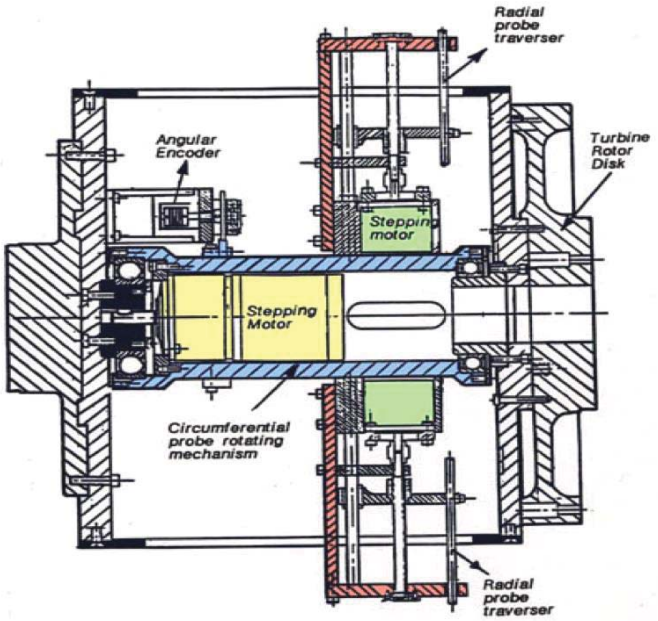

Figure 57: AFTRF Rotating Measurement Schematic.

A stationary-frame radial-circumferential traverse was used as a replacement measurement technique in place of the rotor-relative results that had been included in initial testing plans. Total pressure measurements were acquired with a Kiel probe and a high frequency response pressure probe manufactured by Endevco. When the latter probe results were post processed with a phase-lock averaging method, the total pressure distribution for each individual rotor passage was visible. Distinct fluid structures were observed (e.g. tip vortex, etc.) which enabled a detailed analysis of how fluid structures changed as a function of hardware design variation and rim cavity purge flow rate. This probe proved to be a reasonable replacement for what would have been obtained with rotor-relative measurement techniques.

Measurement uncertainty was estimated for each of the tranducers described above. Estimates of these uncertainties are listed below. Validyne transducers are used for measuring probes in the stationary frame of reference. Thermocouples are used to measure inlet and exit total temperature. Atmospheric pressure is measured using a gage on the wall. The Endevco Probe measures unsteady pressures behind the rotor from the stationary frame. The ZOC22b are used to measure blade and vane loading. The transducer with a one psi operating range is used to measure vane loading, and the more robust 2.5 psi unit measures blade loading from the rotating frame. Probe measurement uncertainties are tabulated in Table 5.

Table 5. Measurement uncertainty for each probe used in this study.

Measurement	Uncertainty
Validyne DP15-30	$\pm 5\ Pa$
K-Type Thermocouple	$\pm 0.2\ K$
Atmospheric Pressure	$\pm 25\ Pa$
Endevco	$\pm 5\ Pa$
ZOC22b-1psi	$\pm 5\ Pa$
ZOC22b-2.5psi	$\pm 15\ Pa$

Moving downstream, the first measurement taken is the inlet velocity. This measurement is used calculate flow coefficient. Inlet velocity is a function of total pressure, static pressure, atmospheric pressure, and temperature. The equation for it is as follows:

$$V_{in} = \sqrt{\frac{2(P_T - P_S)RT}{P_{atm}}}$$

The difference between total and static pressure is measured using one Validyne, meaning that the difference can be treated as one variable. To calculate uncertainty the following equation must be solved:

$$\partial V_{in} = \sqrt{\left(\partial(P_T - P_S)\frac{\partial V_{in}}{\partial(P_T - P_S)}\right)^2 + \left(\partial T\frac{\partial V_{in}}{\partial T}\right)^2 + \left(\partial P_{atm}\frac{\partial V_{in}}{\partial P_{atm}}\right)^2}$$

$$\partial(P_T - P_S) = \pm 5$$

$$\frac{\partial V_{in}}{\partial(P_T - P_S)} = \frac{RT}{P_{atm}\sqrt{\frac{2RT(P_T - P_S)}{P_{atm}}}}$$

$$\partial T = \pm 0.2$$

$$\frac{\partial V_{in}}{\partial T} = \frac{R(P_T - P_S)}{P_{atm}\sqrt{\frac{2RT(P_T - P_S)}{P_{atm}}}}$$

$$\partial P_{atm} = \pm 25$$

$$\frac{\partial V_{in}}{\partial P_{atm}} = \frac{-RT(P_T - P_S)}{P_{atm}^2\sqrt{\frac{2RT(P_T - P_S)}{P_{atm}}}}$$

Inserting values average values into these equation results in a calculated uncertainty. The average amount of error for the inlet velocity is $\pm 0.3\ ^m/_s$.
The next calculation is the vane loading. Since the vanes use the same non-dimensionalization, only one set of calculation will be shown. The difference between the two is only in magnitude of the measurements. Shown below is the equation for the coefficient of static pressure on the vanes and blades. This equation can be simplified by using Bernoulli's principle for the velocity.

$$C_{P,static} = \frac{P_S - P_{atm}}{1/2\,\rho V^2} = \frac{P_S - P_{atm}}{1/2\,\rho \frac{2(P_T - P_S)}{\rho}} = \frac{P_S - P_{atm}}{P_T - P_S}$$

Both the denominator and the numerator are measured with their own respective Validyne. Meaning the equation is only a function of two measurements. To find the uncertainty the following equation is used:

$$\partial C_{P,static} = \sqrt{\left(\partial(P_S - P_{atm})\frac{\partial C_{P,static}}{\partial(P_S - P_{atm})}\right)^2 + \left(\partial(P_T - P_S)\frac{\partial C_{P,static}}{\partial(P_T - P_S)}\right)^2}$$

$$\partial(P_S - P_{atm}) = \partial(P_T - P_S) = \pm 5$$

$$\frac{\partial C_{P,static}}{\partial(P_S - P_{atm})} = \frac{1}{\partial(P_T - P_S)}$$

$$\frac{\partial C_{P,static}}{\partial(P_T - P_S)} = \frac{-(P_S - P_{atm})}{(P_T - P_S)^2}$$

Solving the equation for the vanes gives an uncertainty of ± 0.5, while solving for the blades results in an uncertainty of ± 0.8.

Coefficient of total pressure used for both the Endevco and Kiel type probes behind the rotor, and refered to as $C^*_{P,t}$ within this text, is given by the following equation.

$$C^*_{P,t} = \frac{P_{T,local} - P_{T,in}}{P_{S,exit} - P_{T,in}}$$

$$\partial C^*_{P,t} = \sqrt{\left(\partial\left(P_{T,local} - P_{T,in}\right)\frac{\partial C^*_{P,t}}{\partial\left(P_{T,local} - P_{T,in}\right)}\right)^2 + \left(\partial\left(P_{S,exit} - P_{T,in}\right)\frac{\partial C^*_{P,t}}{\partial\left(P_{S,exit} - P_{T,in}\right)}\right)^2}$$

$$\partial\left(P_{T,local} - P_{T,in}\right) = \partial\left(P_{S,exit} - P_{T,in}\right) = \pm 5$$

$$\frac{\partial C^*_{P,t}}{\partial\left(P_{T,local} - P_{T,in}\right)} = \frac{1}{P_{S,exit} - P_{T,in}}$$

$$\frac{\partial C^*_{P,t}}{\partial\left(P_{S,exit} - P_{T,in}\right)} = -\frac{P_{T,local} - P_{T,in}}{\left(P_{S,exit} - P_{T,in}\right)^2}$$

To find the uncertainty, the worst case scenario is chosen by trying the min and max numbers. But since the numbers are so close together (about 100 pascal difference between the Endevco and Kiel) the resulting uncertainty comes out to be the same. For both the resulting uncertainty in $C^*_{P,t}$is ± 0.002

The Five-Hole Probe's uncertainty is calculated in much the same way. The derived total and static pressure measurements are a function of the five pressure measurements and a calibration

factor. The results of the calculations are presented in Table 6 below, along with the rest of the results of the calculated uncertainties.

Table 6. Derived uncertainty for each calculated variable shown in this study.

Measurement	Uncertainty	Percent
V_{in}	$\pm 0.3\ ^{m}/_{s}$	$\pm 1.88\%$
$C_{P,static}$ Vane	± 0.5	$\pm 3.24\%$
$C_{P,static}$ Blade	± 0.8	$\pm 2.99\%$
$C^{*}_{P,t}$ Kiel	± 0.002	$\pm 0.20\%$
$C^{*}_{P,t}$ Endevco	± 0.002	$\pm 0.20\%$
P_T FHP	$\pm 10\ Pa$	$\pm 0.50\%$
P_S FHP	$\pm 10\ Pa$	$\pm 0.50\%$
V FHP	$\pm 0.75\ ^{m}/_{s}$	$\pm 1.07\%$

AFTRF RESULTS

Vane loadings

Static pressure taps are at three different spanwise locations on three of the inlet vanes and five locations on two of the blades (both baseline and TVC). They are at a constant radius corresponding to 10%, 50%, and 90% span on the vane and 10%, 25%, 50%, 75%, and 90% span on the blades. The equation below shows the definition for static pressure coefficient for the following plots.

$$C_{P,static} = \frac{P_s - P_{atm}}{{}^1\!/_2\,\rho_{in} V_{in}^2}$$

Each pressure plot also contains a numerical prediction provided by P&W. The numerical simulations were conducted with an in-house RANS solver utilizing a laminar to turbulent transition model to capture boundary layer transition behavior.

Figure 58 shows a plot of Cp for the vane at the 10% span location for one of the inlet vanes. The results between the measured and the CFD prediction match fairly well in these cases. The pressure side (upper curve) matches more closely than the suction side (lower curve) of the vanes.

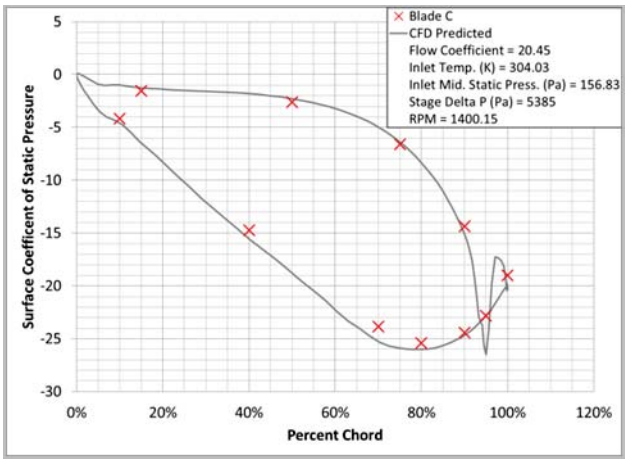

Figure 58: Static Pressure Vane Loading at 50% Span

Blade Loadings

Static pressure loading on the blades is a more challenging measurement than the vane loading. Blade loading must contend with centrifugal pumping in the tubing, pressure drop within the drum, and centrifugal loading on the pressure transducers. Corrections for each of these factors are made to all of the measurements taken in the rotating frame.

Figure 59 shows a plot of Cp from the baseline blade at 10% span. Agreement with the numerical predictions for the suction and pressure surfaces is generally good. At each static tap location there are two symbols representing the two instrumented blades installed on the rotor. At this spanwise position, the two blades show good agreement with each other.

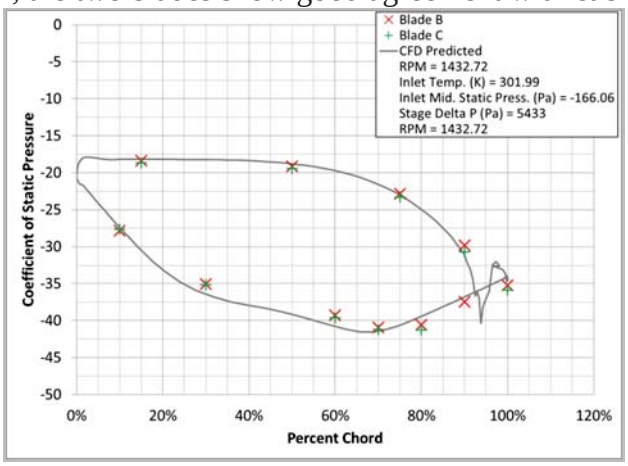

Figure 59: Baseline Rotor Blade Loading at 10% Span

Intraspace Measurements

Vane exit surveys were conducted with a five hole probe and Kiel probe. Positive angle conventions are needed to understand what the FHP is measuring. Figure 60 show that a positive axial direction is downstream, a positive theta direction is counterclockwise, and a positive radial direction is toward the center of rotation. Figure 61 shows the positive angles and the planes they are working in in a ¾ view. Positive alpha would be coming from below the FHP as shown in the blue meridional plane, and positive beta will be coming from the left of the probe shown in the green radial/theta plane. The rotor is represented by the purple oval.

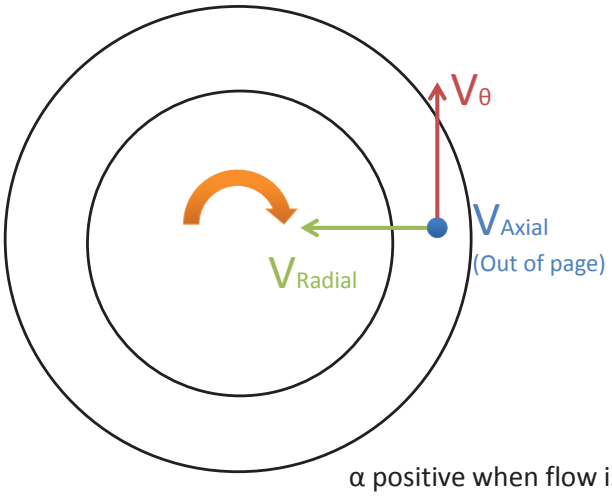

V_{Axial} positive downstream
V_{θ} positive counter clockwise
V_{Radial} positive center of rotation
α positive when flow is moving in positive radial direction
β positive when flow is moving in positive θ direction

Figure 60: Five-Hole Probe Positive Conventions, Downstream of Rotor Looking Toward Inlet

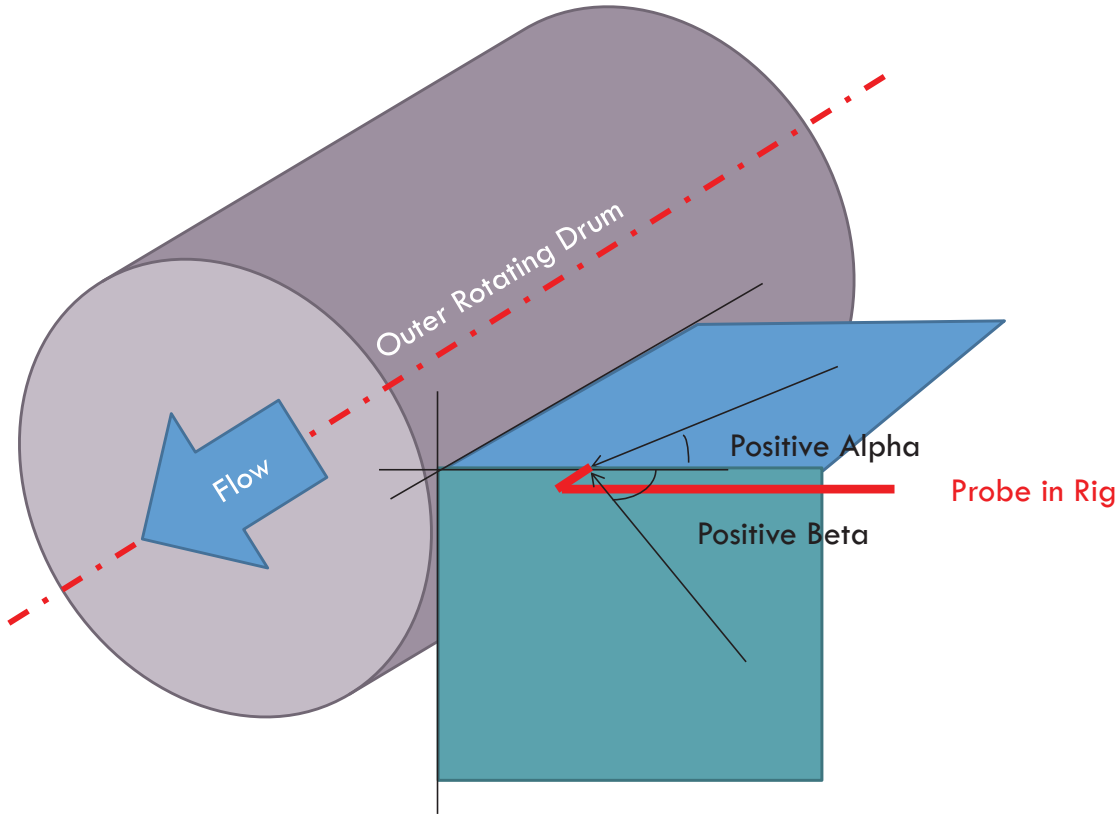

Figure 61: Five-Hole Probe Positive Angle Conventions

Figure 62 shows total pressure coefficient measured from the Kiel at this station. The wake of the vane is clearly visible in the left side of the contours. The passage vortex impact on total pressure loss is visible below 20% span, centered at +1 deg. On the OD endwall, secondary flow impact is visible in the circumferential non-uniformity in boundary layer development.

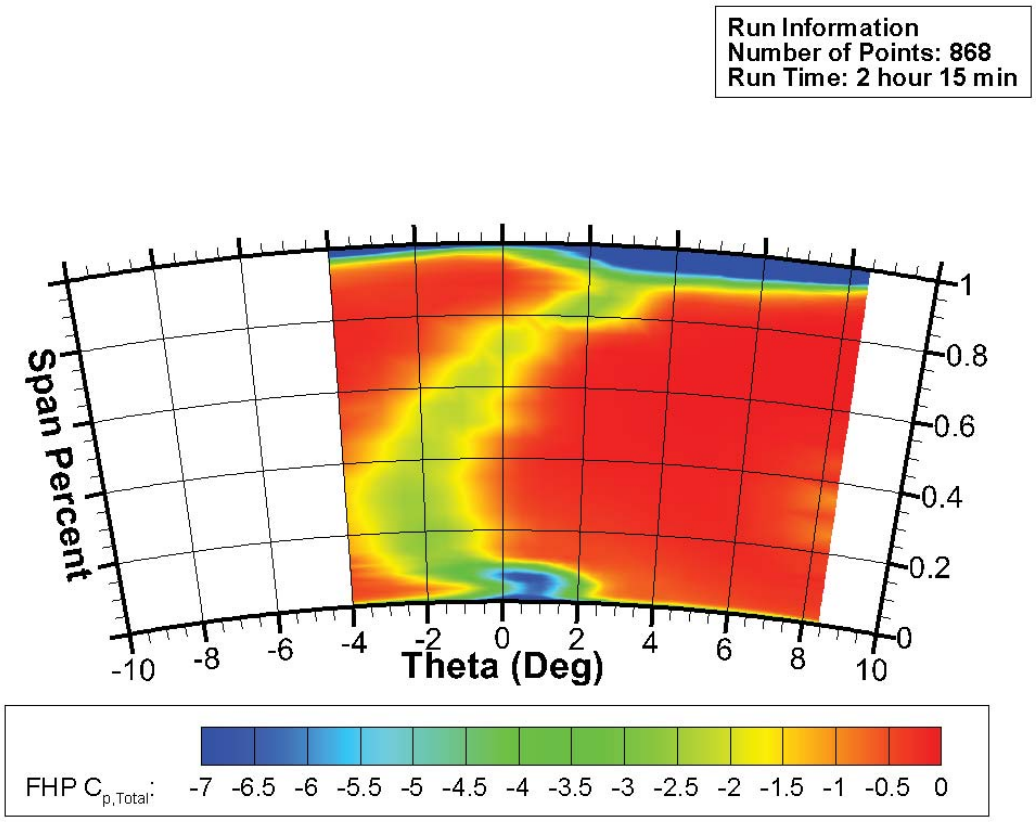

Figure 62: Five-Hole Probe Comparison without Rim-Seal Chamber Installed

Five-Hole Probe Measurements at Vane Exit

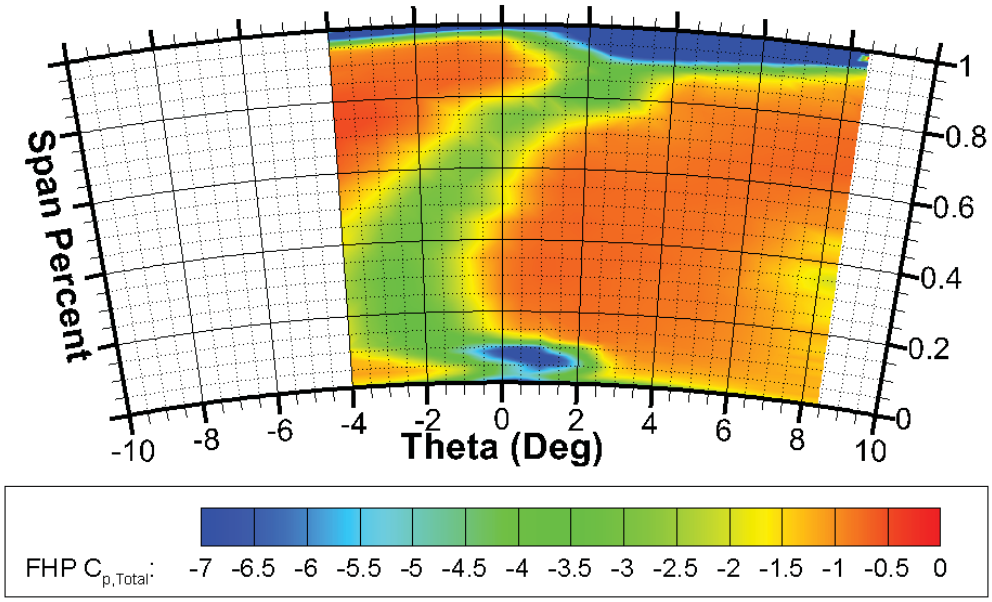

Figure 63: Coefficient of Total Pressure in the Intraspace 868 Point Mesh Measured by a Five-Hole Probe

Figure 63 shows a contour plot of total pressure coefficient as measured by the five hole probe. The flow field corroborates what was measured by the Kiel probe (Figure 62) in that the airfoil wake and endwall structures are clearly identified and in the same positions. The FHP does measure a slightly wider airfoil wake in the region between 20% and 80% span.

Above 90% span is a large region of loss. It is noted that in this region is the window slot for probe access. It is the opinion of the researcher that some of the loss here is due to improper sealing. Improper sealing could induce flows on the probe that are out of acceptable ranges (±30°) on the FHP. A second reason could be due to proximity to the outer casing. The final reason could be due to the fact that the probe is fully or partially recessing into the cavity for these measurements. The large pressure drop in this region could be caused by the probe no longer being completely exposed to the main gas path.

Figure 64 shows the static pressure coefficients at the vane exit plane. Lower static pressure coefficient corresponds to a lower static pressure. The radial distribution characteristic of a swirling annular flow is clearly visible. Circumferential variations in static pressure are a result of the vane potential field extending downstream of the vane trailing edge.

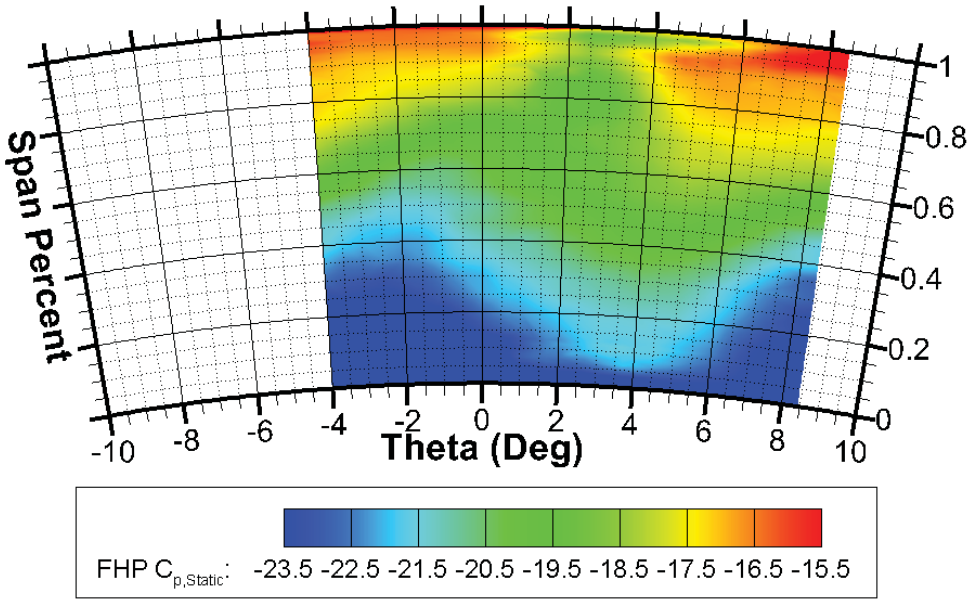

Figure 64: Coefficient of Static Pressure in the Intraspace 868 Point Mesh Measured by a Five-Hole Probe

Blade Exit Measurements

The baseline blade was used to demonstrate the new rig hardware. Measurements downstream of the blade were taken with a Kiel probe and with an Endevco probe. The measured total pressure coefficient, Cp,total* is defined as:

$$C^*_{P,total} = \frac{P_{t,local} - P_{t,in}}{P_{s,exit} - P_{t,in}}.$$

Endevco measurements were taken at zero rim cavity purge flow rate. These results are shown in Figure 65. These contours of total pressure coefficient were, first, phase-lock averaged to obtain a full wheel measurement map of the full rotor, and then passage-averaged to eliminate circumferential measurement variations that were present in the Endevco results. This figure shows the final passage-averaged contours.

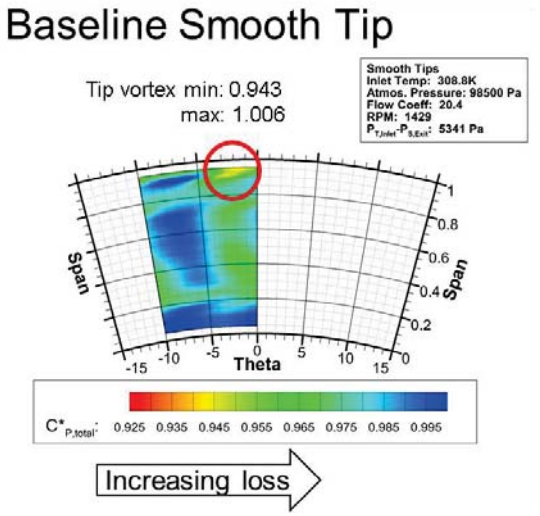

Figure 65: Contours of average total pressure coefficient from the Endevco probe

Purge Flow Impact on Rotor Exit: Kiel Measurements

Purge flow was introduced into the rim-seal cavity at four different rates. The rates are carefully monitored using an ASME calibrated orifice and total pressure contour maps are taken for each case. The variation in purge flow rate for these tests is tabulated in Table 7. Purge rate percentages are relative to the main gas path flow rate.

Table 7: Rim cavity purge flow rate test matrix

Blade Type	Tip Style	Purge Rate
Baseline	Smooth	0.00%
		0.25%
		0.50%
		1.00%

These flows were measured with the stationary-frame Kiel probe. The Kiel was radially traversed downstream of the rotor. The resulting time averaged data is shown as radial profiles of total pressure coefficient in Figure 66. Increasing purge flow rate increases the secondary flow penetration height through the passage.

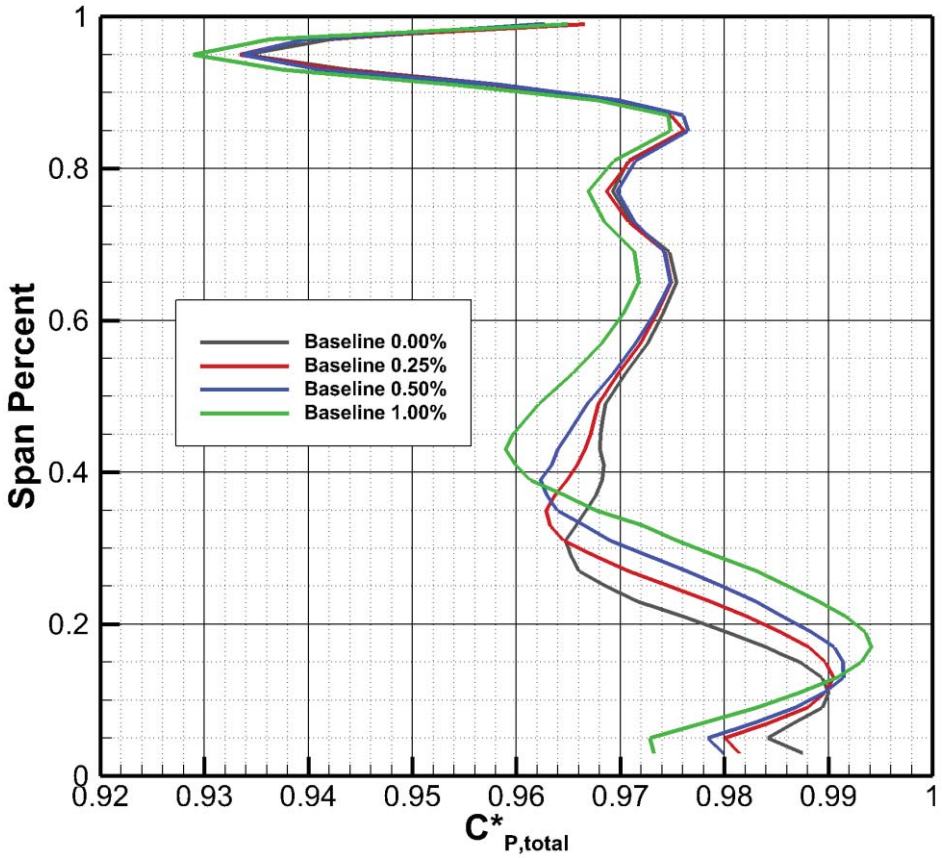

Figure 66: Baseline Blade Purge Varying Purge Rate

4 Summary Of Contract Data Deliverables

Task	Description	Status
1	**Low Speed Cascade Facility Modification**	
	New vane geometry	Complete
	Bluff body geometry which is clockable	Complete
	Provisions for upstream and downstream leakage	Yes, only using downstream
2	**Instrument LSC Hardware and Test Section**	
	Optical access for LDV, PIV	Yes
	Static pressure taps	Yes
	5-hole pressure probe	Yes
	Surface TC's	Yes
	Thermocouple probes	Yes
	As required for measuring:	-
	Aero loss	Yes, 5-hole probe
	Steady Ps	Yes, Ptaps
	Unsteady Ps	No, determined not needed
	Rim cavity effectiveness	IR thermography, TC rakes, CO2
3	**AFTRF Modification**	
	Modify existing baseline stage for receiving vanes, blades, and rim cavities as req'd	Complete
	Install rim cavity	Complete
	Design, build, assemble a new intra-stage traverse for detailed flow measurements	Complete
	Design, build, assemble a new rotor exit traverse that moves both radial and circumferential	Complete
	Modify rotating instrumentation package	Complete
	Improve and assemble a modified phase-locked and time accurate rotor exit total prssure mapping system	Complete
	Design and build a new measurement system based on stage inlet and exit for measuring efficiency	Complete
4	**Instrument AFTRF Hardware**	
	Rotating frame measurements	Yes
	High response instrumentation	Yes, Endevco
	Hot wire	Yes
	Conventional probes	Yes
	Pressure taps in flowpath and rim cavity	Yes
	As required for measuring:	-
	Flowpath and rim cavity flow fields using high response radial/circumferential traversing probes	Yes
	Steady and unsteady airfoil, platform, and rim cavity surface static pressures	Yes
	Rim cavity effectiveness (ingestion)	No

Task	Description	Status
5	**LSC Testing**	
	Experimental measurements on 12 or more configurations (including blade, vane, endwall, cavity, and clocking changes).	Complete
	Measure aerodynamic losses	Complete
	Measure steady airfoil, platform, and rim cavity surface static pressures	Complete
	Measure rim cavity ingestion effectiveness	Complete
6	**Baseline AFTRF Test**	
	Shake down and baseline geometry testing to be used for comparing optimized geometries tested later.	Complete
7	**LSC Testing**	
	Experimental measurments on 4 or more configurations (including blade, vane, endwall, cavity, and clocking changes).	(1) Baseline (2) Baseline with bluff bodies (3) Long-Combined Endwall (4) Long Vane Endwall
	Measure aerodynamic losses	In-Progress
	Flowfield measurements (PIV or LDV)	Complete
8	**AFTRF Testing**	
	Experimental measurments on 3 or more configurations.	(1) Grooved baseline tip (2) TVC Blade (3) Grooved TVC tip (4) New rim-seal geometry
	Flowfield measurements using high response radial/circumferential traversing probes	Endevco and Kiel
	Steady and unsteady airfoil, platform, and rim cavity surface static pressures	Complete
	Rim cavity ingestion effectiveness	No

5 CONCLUSIONS

LSC:

- Trend-accurate low speed cascade.
- Matches upstream and downstream pressure field of the rim-cavity exit.
- A place to test concepts in a region of the engine where CFD solutions are still being developed.
- Cascade results show that extending the vane trailing edge of the seal provides benefit and extending the blade leading edge of the seal does not provide benefit. Benefit is improved seal effectiveness (reduced ingestion and purge flow cooling on downstream platform).
- Cascade results are insensitive to location of downstream bluff body

AFTRF:

- New low-speed rig geometry installed, matched CFD airfoil loadings
- Increasing purge flow in low speed rig pushes ID loss from horseshoe vortex radially outward.

APPENDIX: TEST ARTICLE PHOTOS

AFTRF

AFTRF assembled vane ring. The cut-away in the case in the upper right corner is where the optical access port is located.

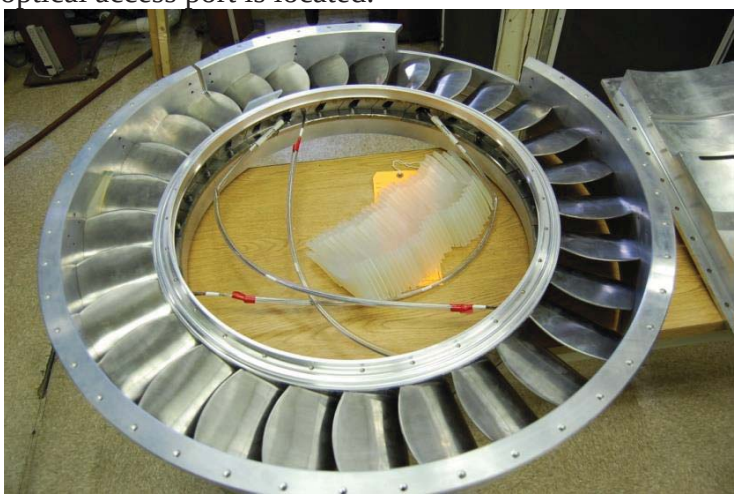

AFTRF traverse and port cover.

AFTRF assembled blades and rotor.

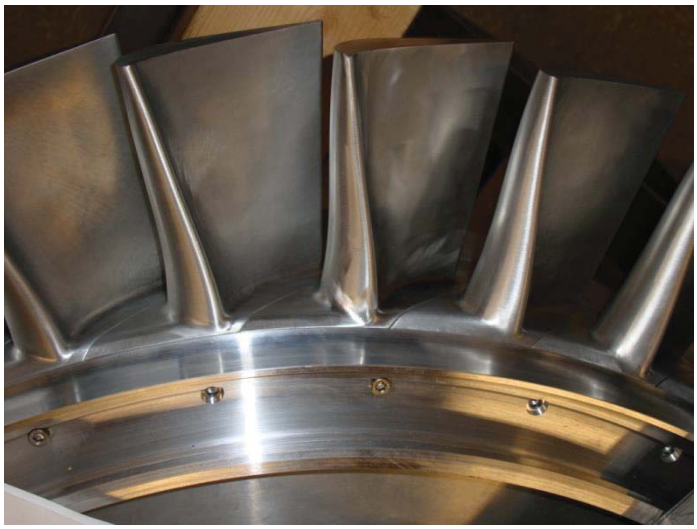

LSC

LSC instrumented vane (static pressure tap leads)

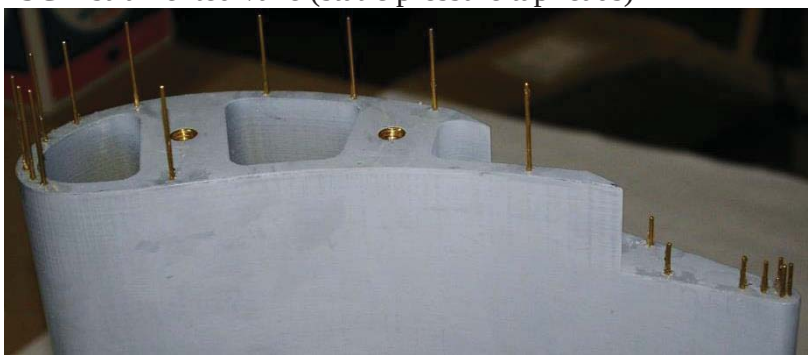

LSC vane endwall and upstream rim cavity, showing vane cut-away and thermocouple rakes installed in the rim cavity.

6 REFERENCES

Gibson J., Thole K., Christophel J., Memory C., 2015 “Effects of the Main Gas Path Pressure Field on Rim Seal Flows in a Stationary Linear Cascade,” ASME Paper No. 2015-43517